Combust. Sci. and Tech., 180: 89–126, 2008

ISSN: 0010-2202 print/1563-521X online
DOI: 10.1080/00102200701487087

Taylor & Francis
Taylor & Francis Group

IGNITION AND EXTINCTION IN CATALYTIC PARTIAL OXIDATION OF METHANE-OXYGEN MIXTURES WITH LARGE H_2O AND CO_2 DILUTION

Adrian Schneider[1], John Mantzaras[1,*], and Sara Eriksson[2]
[1]*Paul Scherrer Institute, Combustion Research, CH-5232 Villigen PSI, Switzerland*
[2]*Royal Institute of Technology, Chemical Technology, Teknikringen, Stockholm, Sweden*

The ignition and extinction in catalytic partial oxidation (CPO) of CH_4/O_2 mixtures with large exhaust gas dilution (46.3% H_2O and 23.1% CO_2 vol.) has been investigated experimentally and numerically at 5 bar. Experiments were carried out in a short contact time Rh-coated honeycomb reactor and involved temperature measurements along the reactor and exhaust gas analysis. Numerical predictions were performed with a 2-D transient elliptic code that included detailed chemical reaction schemes and relevant heat transfer mechanisms in the solid. The employed heterogeneous reaction scheme reproduced the measured minimum inlet temperatures required for catalytic ignition (light-off), the elapsed times for the propagation of the reaction front, and the steady-state exhaust gas compositions at a fuel-to-air equivalence ratio of $\varphi = 4.0$. The chemical impact of the added H_2O, although important already at the early light-off stages, was minimal on the ignition delay times because the latter were dominated by total oxidation and not by partial oxidation or reforming reactions. The key reaction controlling catalytic ignition was the surface oxidation of CO to CO_2, which was the main exothermic heat release step in the induction zone. Measurements and predictions indicated that vigorous combustion could be sustained at inlet temperatures at least as low as 473 K and 298 K in CPO with and without exhaust gas dilution, respectively. The extended stability limits of CPO combustion were due to a shift from partial to total oxidation products, and hence to higher exothermicity, with decreasing inlet temperature. The key parameter controlling extinction was the CO(s) coverage, which led to catalyst poisoning. Finally, operation at non-optimal stoichiometries ($\varphi = 2.5$) was shown to be beneficial in CPO of power generation systems with large exhaust dilution, due to the moderating effect of dilution on the maximum reactor temperature.

Keywords: Catalytic ignition and extinction; Catalytic partial oxidation of methane; Exhaust gas dilution; Transient reacting flow modeling

Received 12 December 2006; accepted 29 May 2007.
Support was provided by the Swiss Federal Office of Energy (BFE), Swiss Federal Office of Education and Science (BBW) through the European Union project Advanced Zero Emissions Power and ALSTOM of Switzerland. The help of Mr. Rolf Schaeren in the experiments is gratefully acknowledged.
*Address correspondence to ioannis.mantzaras@psi.ch

INTRODUCTION

The catalytic partial oxidation (CPO) of natural gas to synthesis gas has attracted increased attention in gas turbines of power generation systems (Karim et al., 2002; Griffin et al., 2004). The adopted approach, referred to as "catalytic rich combustion," entails CPO of natural gas with part of the air stream (at suitably fuel-rich stoichiometries) in a short contact time reactor. Only a fraction of the fuel is converted in the CPO reactor, while the products (mainly synthesis gas and unconverted methane) are subsequently mixed with the remaining air to stabilize a post-catalyst fuel-lean homogeneous (gas-phase) combustion zone. The aforementioned methodology has a number of advantages compared to the conventional fuel-lean catalytically stabilized combustion (Carroni et al., 2002), the two most prominent ones being the lower catalyst light-off temperature (Veser et al., 1999) and the enhanced stability of the follow-up flame due to the CPO-produced hydrogen (Griffin et al., 2004). Even though "catalytic rich combustion" usually applies to natural-gas/air mixtures, the use of large exhaust gas recycle (EGR) in the feed is under investigation for new power generation cycles. Such an example is the advanced zero-emissions power cycle (Griffin et al., 2005) that aims at mitigating both NO_x and CO_2 emissions. Therein natural gas is combusted at moderate temperatures (up to 1500 K) in a stream comprising oxygen (separated from air) and large EGR (up to 80%vol.). Combustion in pure oxygen negates the formation of NO_x, while the lack of nitrogen in the flue gases allows for an efficient separation of CO_2 from H_2O (e.g., via condensation) thus facilitating the subsequent sequestration of CO_2.

Due to its key role in the chemical industry, the CPO of methane (the main constituent of natural gas) has been intensely studied during the last years, with emphasis on understanding the heterogeneous kinetics over Pt and Rh surfaces and the synthesis gas yields in short contact time reactors (Hickman and Schmidt, 1993; Bodke et al., 1998; Deutschmann and Schmidt, 1998; Aghalayam et al., 2003; Schwiedernoch et al., 2003). The CPO processes in power generation are, nonetheless, differentiated from those of the chemical industry. A fractional fuel conversion is sufficient in the former, whereas complete conversion is desired in the latter. In addition, the optimization of product yields and selectivities is not an overriding issue in power generation since CO is ultimately converted to CO_2 and the amount of hydrogen should simply suffice for the stabilization of the follow-up flame. Conversely, in gas turbines there are stringent catalyst light-off requirements ($\sim$700 K or less) at gas hourly space velocities (GHSV) of $\sim 10^6\,h^{-1}$. To advance the understanding of "catalytic rich combustion," Appel et al. (2005) have recently studied the underlying heterogeneous processes in CPO of CH_4/air over Rh/ZrO_2 at 6 bars by applying laser-based in situ Raman measurements of major gas-phase species concentrations over the catalyst boundary layer. In the same study, the validated kinetic schemes were also used to simulate the steady operation of a prototype subscale gas turbine reactor. More recently, Schneider et al. (2007) investigated the hetero-/homogeneous kinetics in CPO of methane with large EGR at pressures of 4 to 10 bar by employing Raman measurements of major species concentrations and laser-induced fluorescence (LIF) of formaldehyde. The steady performance of a subscale gas turbine reactor and the chemical impact of large H_2O and CO_2 dilution on

the synthesis gas yields and selectivities were further addressed in Schneider et al. (2006).

Dynamic performance in gas-turbine-related CPO has not been elaborated in the past. Light-off, in particular, is crucial given the strict limitations in reactor inlet temperature. Extinction is also a key issue, especially for low part-load and idle turbine operation. Recent experiments have reported an extended hysteresis in the ignition/extinction characteristics of methane CPO with EGR (Schneider et al., 2006). Similarly, strong hysteresis has been observed in CPO of methane, landfill gas, and diesel fuels with air (Smith et al., 2006). The reason for this behavior, which is in marked contrast to fuel-lean catalytic combustion, has not yet been clarified.

Transient models are of great interest for the description of dynamic operation in practical catalytic systems and also for the fundamental investigation of kinetically driven dynamic oscillatory phenomena (Imbihl and Ertl, 1995). Given the typically long characteristic solid substrate heat-up time compared to the corresponding chemical, convective and gas diffusive time scales, the quasi-steady assumption for the gas-phase is usually invoked. This is the preferred approach in demanding (even when simplified surface chemistry is used) 2-D transient channel simulations (Sinha et al., 1985). The quasi-steady approximation has also been applied in continuum 2-D models for the entire honeycomb structure (Zygourakis, 1989; Schwiedernoch et al., 2002). These models are of great interest for practical systems with non-adiabatic operation and non-uniform inlet properties, but they do not resolve the details in the solid wall of each channel and they require careful assessment of effective continuum properties for the solid structure.

Transient simulations for both the solid and gas phases, with the added complexity of detailed surface chemistry, have only been reported for 1-D models with lumped heat and mass transport coefficients (Kramer et al., 2002). Despite the computational efficiency of 1-D approaches, 2-D models have the advantage of accurately describing the interphase transport and the gas-phase chemical processes; the latter are strongly dependent on the cross-flow distribution of species and temperature and can become increasingly important at elevated pressures (Mantzaras, 2006). For methane CPO, in particular, 1-D transient modeling has been carried out in Veser and Frauhammer (2000) for Pt catalysts, and 2-D continuum modeling in Schwiedernoch et al. (2003) for Rh catalysts; both studies employed detailed surface reaction mechanisms. Transient 2-D models with detailed chemistry have not yet been reported for single catalytic channels.

An experimental and numerical study of methane CPO is undertaken in this article, with emphasis on light-off and extinction. Light-off has been investigated in CPO with large EGR (up to 75%vol.) whereas extinction has been studied in CPO with and without EGR. Transient and steady experiments have been carried out at pressures of 5 and 3 bar in a short contact time ($\sim$10 ms) subscale gas-turbine catalytic reactor coated with Rh/ZrO_2. The exhaust composition was monitored with gas chromatography, while the inlet, outlet, and reactor temperatures were measured with thermocouples. An elliptic 2-D transient model for a single channel has been developed, which included detailed hetero/homogeneous chemical reaction schemes and all relevant heat transfer mechanisms in the solid. The main objectives were to validate the aptness of heterogeneous reaction mechanisms during ignition/extinction in CPO of methane with large EGR, to identify the chemical

pathways controlling catalytic ignition and extinction, and to understand the origin of the extended extinction limits of short contact time reactors. Particular objectives were to address design issues for transient performance of CPO reactors with large EGR.

The high-pressure test rig and the numerical methodology are introduced first. Comparisons between measured and predicted ignition characteristics in CPO of $CH_4/O_2/H_2O/CO_2$ mixtures are then presented and the chemical pathways controlling light-off are identified. The extinction in CPO of $CH_4/O_2/H_2O/CO_2$ and $CH_4/O_2/N_2$ mixtures is finally elaborated and the associated key chemical pathways are clarified.

EXPERIMENTAL

High Pressure Test Rig

The short contact time honeycomb catalytic reactor was a subscale unit of a prototype CPO burner developed for large gas turbines (Griffin et al., 2004) and was embedded inside a high-pressure tank (Figure 1a). The same reactor type has also been used in earlier heterogeneous studies of methane, which included total

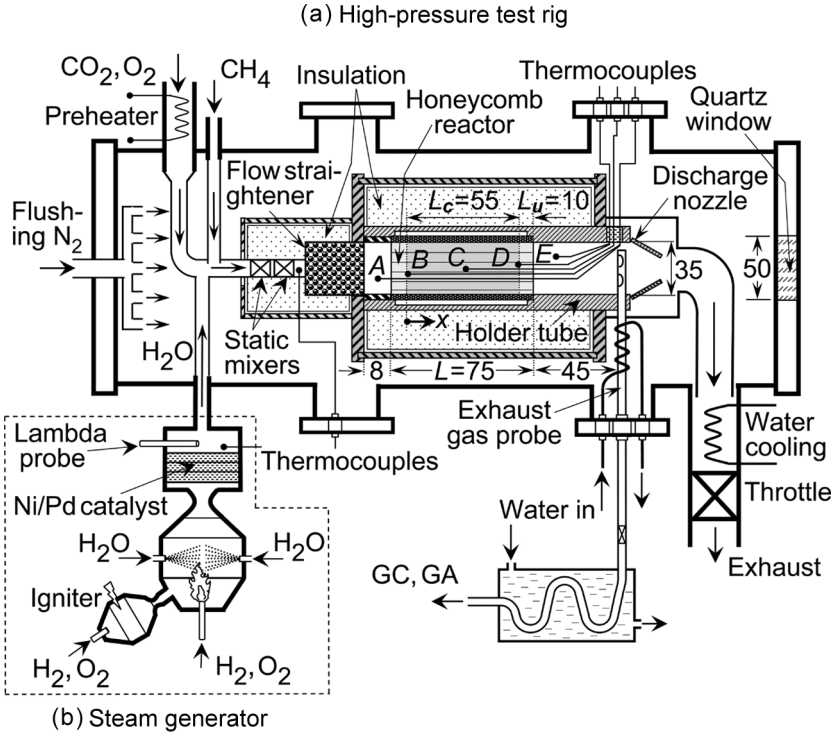

Figure 1 (a) High-pressure catalytic partial oxidation test rig, configured for operation with simulated exhaust gas recycle, (b) steam generator. All distances are in mm.

oxidation over Pd (Carroni et al., 2003) and partial oxidation over Rh/ZrO_2 (Schneider et al., 2006). It comprised a 35 mm inner-diameter, 75 mm long and 1.5 mm thick steel tube, wherein alternating flat and corrugated FeCr-alloy foils (with thickness $\delta = 50\,\mu m$) created a honeycomb structure. The cross section of each channel was trapezoidal with rounded corners and the equivalent hydraulic radius was $r_h = 0.6\,mm$. The reactor was mounted inside a well-insulated (using a 30-mm-thick fiber ceramic material) cylindrical steel frame. Only the central reactor extent ($L_c = 55\,mm$) was coated with a catalyst, while the end-sections (each with a length $L_u = 10\,mm$) were catalytically inactive (see Figure 1a).

The inlet, outlet and reactor temperatures were monitored with five 50-μm-thick K-type (Ni/Cr-Ni/Al) sheathed thermocouples (designated as *A* to *E* in Figure 1a). The thermocouple beads were positioned at $x = -15$, 0, 27, 55 and 75 mm, with $x = 0$ denoting the beginning of the catalytic section. The 0.8-mm-thick carrying wires of thermocouples *A* to *D* were driven into the reactor counterflow, through four honeycomb channels (Figure 1a). The three thermocouples inside the honeycomb structure (*B*, *C* and *D*) provided neither the true catalyst surface temperature nor the mean gas temperature but rather a weighted average, which was only indicative of the local reactor temperature. Of the 2 measured true local gas temperatures (*A*, *E*), radiation corrections (amounting up to 8 K) have only been applied to the inlet thermocouple (*A*) that had a direct view to the hot catalyst entry; no such corrections were necessary for the outlet thermocouple (*E*) due to the small differences between the exit gas and rear reactor wall temperatures ($\sim$20 K). The absolute accuracy of the gas temperature measurements was ± 10 K for the hot outlet and ± 6 K for the inlet.

To simulate EGR, a dedicated steam-generator supplied superheated steam (Figure 1b). Details of this unit have been provided elsewhere (Schneider et al., 2006) and only a brief description is given here. The device comprised a spark-ignited H_2/O_2 preburner, whose combustion products ignited a main H_2/O_2 burner. The latter was operated slightly fuel-lean ($\varphi \approx 0.99$), so as to avoid potential hydrogen breakthrough, by using the feedback control of a lambda probe similar to that used in automotive systems. The combustion heat was in turn used to vaporize accurately measured amounts of demineralized liquid water. The degree of superheat and the amount of steam could be independently controlled (up to 1000°C and 20 g/s, respectively). Finally, a Ni/Pd-coated foam positioned downstream of the main burner served as safety backup to convert any escaping hydrogen and to assure a high degree of steam purity.

For the CPO tests of CH_4/O_2 with EGR, high-pressure bottles supplied CO_2, O_2 and technical-grade CH_4 (>99.5%). Three Brooks mass flow-meters regulated the corresponding flows, leading to equivalence ratio accuracies better than $\pm 0.5\%$. The CO_2 and O_2 flows were preheated by a 3 kW resistive heater and then mixed with superheated steam and room-temperature methane in 2 sequential static mixers (Figure 1a). A follow-up 40-mm-long packing of 2-mm-diameter ceramic spheres straightened the flow. A K-type thermocouple positioned downstream of the static mixers monitored the gas temperature, which was in turn used as a feedback to control the level of CO_2/O_2 preheat and the degree of steam superheat for a desired mixture temperature at the reactor inlet. For the CPO tests with $CH_4/O_2/N_2$ mixtures (without EGR), nitrogen was supplied by high-pressure

bottles and regulated by a Brooks mass flowmeter; the N_2 and O_2 gases were pre-heated in the aforementioned resistive heater and finally mixed with methane before entering the reactor.

The honeycomb structure was affixed 8 mm downstream of the flow straightener and was mounted inside a 2.5 mm thick and 35 mm internal diameter steel holder tube. To further minimize heat losses, only the first and last 2 mm of the reactor contacted the holder tube, while in the remaining length a 1-mm-thick annular air-cushion was available. The holder tube ended at a discharge nozzle that directed the flue gases first to an exhaust pipe and then to a water-cooled outlet of the high pressure tank.

The high-pressure tank that housed the reactor was a stainless-steel cylindrical structure with a length of 1.8 m and an internal diameter of 0.28 m. The same tank has also accommodated an optically accessible catalytic reactor in earlier hetero-/homogeneous kinetic studies (Reinke et al., 2004; Appel et al., 2005; Reinke et al., 2005; Schneider et al., 2007). For safety reasons, the exhaust gases were diluted with flushing nitrogen that flowed continuously in the free volume between the high-pressure tank and the reactor. Visual inspection of the reactor assembly was achieved via a 50 mm diameter quartz window at the rear flange of the tank (Figure 1a) and two 350 mm long and 50 mm high quartz windows at the tank sides (not shown in Figure 1a). The gas sampling probe with its associated water cooling lines (see discussion in next section) and the thermocouple wires were driven inside the tank through high-pressure fittings mounted on 4 flanges.

The experimental conditions are provided in Table 1. Cases 1 to 9 referred to CPO of CH_4/O_2 with 69.4%vol. EGR dilution (46.3% H_2O and 23.1% CO_2) and a CH_4 to O_2 equivalence ratio (φ) of 4; in Case 10 the EGR dilution was 75% vol. and $\varphi = 2.5$. Cases 11 to 14 referred to CPO of $CH_4/O_2/N_2$ mixtures with an O_2 to N_2

Table 1 Experimental conditions[(a)]

Case	Type	ϕ	p (bar)	U_{IN} (m/s)	T_{IN} (K)	CH_4 (%)	O_2 (%)	H_2O (%)	CO_2 (%)	N_2 (%)	Catalyst Rh wt%	B[(b)]
1	Ign.	4.0	5	5.6	680	20.4	10.2	46.3	23.1	–	1.0	4.5
2	Ext.	4.0	5	5.1	623	20.4	10.2	46.3	23.1	–	1.0	4.5
3	Ext.	4.0	5	4.7	573	20.4	10.2	46.3	23.1	–	1.0	4.5
4	Ext.	4.0	5	4.3	523	20.4	10.2	46.3	23.1	–	1.0	4.5
5	Ext.	4.0	5	3.9	473	20.4	10.2	46.3	23.1	–	1.0	4.5
6	Ign.	4.0	5	6.0	730	20.4	10.2	46.3	23.1	–	0.5	3.0
7	Ext.	4.0	5	5.1	623	20.4	10.2	46.3	23.1	–	0.5	3.0
8	Ext.	4.0	5	4.3	523	20.4	10.2	46.3	23.1	–	0.5	3.0
9	Ext.	4.0	5	3.9	473	20.4	10.2	46.3	23.1	–	0.5	3.0
10	Ign.	2.5	5	5.5	725	13.9	11.1	50.0	25.0	–	1.0	4.5
11	Ext.	4.0	3	5.4	552	27.7	13.9	–	–	58.4	1.0	4.5
12	Ext.	4.0	3	4.5	470	27.7	13.9	–	–	58.4	1.0	4.5
13	Ext.	4.0	3	4.0	414	27.7	13.9	–	–	58.4	1.0	4.5
14	Ext.	4.0	3	2.9	298	27.7	13.9	–	–	58.4	1.0	4.5

[(a)]Type of test (ignition, extinction-related), equivalence ratio, pressure, inlet conditions and volumetric composition, rhodium loading in catalyst, ratio of active-to-geometrical surface area.

[(b)]The ratio B (active to geometrical area) corresponds to a catalyst dispersion of 25.9 m^2/g-Rh for the 1% wt Rh loading and to 34.5 m^2/g-Rh for the 0.5% wt Rh loading.

molar ratio of 0.24. In Cases 1 to 9 the pressure was 5 bar and the mass throughput ($\rho_{IN} U_{IN}$) was maintained constant. The CPO tests without EGR (Cases 11 to 14) were carried out at 3 bar, again at a constant mass throughput. Laminar flows were established in all cases, with incoming Reynolds numbers less than 580 in each individual channel of the honeycomb reactor. The computed residence times (accounting for flow acceleration due to heating) ranged from 8.8 to 11.9 ms. The gas hourly space velocity (ratio of the incoming volumetric flow rate, at standard conditions, to the volume of the coated reactor section) was $7.4 \times 10^5\,h^{-1}$ in Cases 1 to 9, $6.9 \times 10^5\,h^{-1}$ in Case 10 and $5.2 \times 10^5\,h^{-1}$ in Cases 11 to 14, which were realistically high for gas-turbine CPO systems.

Light-off tests were carried out only for CPO with EGR, in Cases 1, 6 and 10. Therein, the inlet mixture compositions were first established in the reactor at inlet temperatures (T_{IN}) about 100 K lower than those of Table 1. The inlet temperatures were then ramped at a rate of $+10\,K/min$ so as to reach the value required to achieve catalytic ignition. Once light-off was achieved and steady operation was reached in Cases 1 and 6, extinction was subsequently investigated by reducing the inlet temperatures at a rate of 10 K/min. At certain inlet temperatures, steady states were established for periods as long as 15 min to accommodate gas-analysis measurements. Of those steady states, Cases 2 to 5 (pertaining to Case 1) and Cases 7 to 9 (pertaining to Case 6) will be presented herein. In the $CH_4/O_2/N_2$ extinction studies (Cases 11 to 14), steady combustion was first established at the conditions of Case 1; the steam generator was then turned off, nitrogen was added, and the corresponding CH_4, O_2 and N_2 flows were adjusted to achieve the composition of Table 1. Finally, data acquisition, reactor operation and safety control were achieved with dedicated software running on a PC at 1 Hz. This frequency was still sufficient for the ignition studies, characterized by light-off times of up to 10 sec.

Gas Analysis

Gas analysis was carried out in all steady cases; gas compositions could not be resolved over the short ignition events. Part of the exhaust gas was sampled with a water-cooled, silica-coated steel probe, which was positioned 45 mm downstream of the honeycomb (Figure 1a). The steam of the sampled gas was condensed in a water-cooled serpentine heat exchanger outside the tank. The dried gases entered a rack of gas analyzers (GA) and also the sample port of a gas chromatograph (GC). Removal of the steam was necessary for the proper operation of both analysis instruments. Nonetheless, the compositions of the actual wet gas products could still be determined by calculating the element balances.

The Hartmann and Braun gas analyzers Uras-10E for CO (NDIR), Magnos-6G for O_2 (paramagnetic) and Caldos-5G for H_2 (thermal-conductivity-based) were used in a continuous mode. The accuracy of the GA measurements has been determined with calibration gas mixtures and was particularly good for CO (0.3% relative error for typical 10–14% vol. CO in the dry gas), while the O_2 accuracy was still acceptable despite the scarce amounts of this compound (20% relative error for $\sim$1% vol. O_2). The presence of flue gases with thermal conductivities considerably different than that of the reference nitrogen (e.g., CH_4 and CO_2) resulted in larger inaccuracies for hydrogen (20% relative error for typical 25–30% vol. H_2 in the

dry gas). This effect has been partly compensated by calibrating the device with simulated exhaust gas mixtures. In parallel to the GA measurements, more detailed analysis was carried out in an HP-6890++ GC equipped with porous polymer and molecular sieve columns and a thermal conductivity sensor. The GC further allowed for measurements of CH_4, CO_2 and N_2. The porous polymer column separated CO_2 before the gas entered the molecular sieve. Helium was the carrier gas, while the analysis was discontinuous with one measurement every 8 min. The GC has been tested against a selection of different calibration gas mixtures. Even though the hydrogen signals were weak due to the choice of helium as carrier gas, for the substantial H_2 amounts of the present work the accuracy was good (relative error for H_2 $\sim$4%). The relative error in the GC measurements of the other species was less than 5% for CH_4, CO_2, CO and N_2, increasing up to 50% for the scarce O_2. In the forthcoming sections only the GC measurements are presented; the GA data have provided an additional (and successful) control, mainly for the CO and O_2 compositions.

Catalyst Preparation and Characterization

The ZrO_2 support material was calcined at 1073 K for 5 h. The catalyst contained 1% wt Rh (0.5% wt in Cases 6 to 9) and was prepared by incipient wetness impregnation of the ZrO_2 support with aqueous solutions of $Rh(NO_3)_3$. The impregnated supports were dried at 383 K, followed by calcination at 873 K for 5 h. A slurry of the catalyst powder was then sprayed into the FeCr-alloy foils and the coated structures were further calcined at 873 K for 1 h. Four successive layers were applied, resulting in a catalyst thickness $\delta_c = 4.6\,\mu m$. Before each combustion run, the catalyst was reduced in a 673 K flow of H_2/N_2 for 20 min.

The total and active areas of both fresh and used FeCr-alloy foils were measured with BET (N_2-physisorption) and H_2-chemisorption. Hydrogen chemisorption analysis was performed on a Quantachrome Autosorb-1C to determine the noble metal dispersion. The hydrogen adsorption measurements were carried out at 195 K and the data analysis considered a H_2:Rh stoichiometry of 1:2. The metal dispersion was calculated according to the dual isotherm method: after determining the first isotherm, the sample was evacuated and a second isotherm was obtained. The second isotherm represented only physisorbed H_2. Thus, the difference between the two isotherms corresponded to the amount of chemisorbed hydrogen. The ratio of active-to-geometrical surface area (B), which was deduced from the chemisorption-measured catalyst dispersion, was a parameter needed in the numerical model (see Table 1 and footnote (b)). Supplementary surface science measurements were also made (surface Raman and X-ray photoelectron spectroscopy to identify the crystal structure and oxidation state of the surface species, respectively), but they were of limited interest for the present study; those measurements have been reported elsewhere (Eriksson et al., 2006).

NUMERICAL

Given the good thermal insulation and the uniform properties at the front face of the honeycomb (see also discussion in section "Boundary conditions and method

Table 2 Properties of solid[(a)]

Material	T (K)	λ(W/mK)	ρ(kg/m^3)	c (J/kgK)[(b)]
FeCr	680	16	7200	615
FeCr	1100	16	7200	940
ZrO_2[(c)]	680	0.45	3560	590
ZrO_2	1100	0.52	3540	695

[(a)]Thermal conductivity, density, heat capacity at two selected temperatures.
[(b)]In the range 600–1200 K, $c_{FeCr} = b_0 + b_1 T + b_2 T^2, b_0 = 580,\ b_1 = 0.394$ and $b_2 = 6.57\text{x}10^{-4}$.
[(c)]The properties of ZrO_2 have been corrected for porosity (37%, assessed from the physisorption tests).

of solution''), a single-channel model has been constructed. A representative channel was treated as a cylindrical tube with inner radius $r_h = 0.6$ mm. This was a reasonable simplification given the lack of prevailing secondary flows (straight channels having trapezoidal cross sections with rounded corners), as also reported in Schneider et al. (2006). A full elliptic 2-D quasi-steady model was employed for the reactive gas flow. On the other hand, the spatial dimensionality of the solid was dictated by characteristic time considerations. The characteristic time for axial convection was, as discussed in the experimental section, $t_{g,x} \sim (9\text{-}12) \times 10^{-3}$ s, while the characteristic time for radial gas diffusion ($r_h{}^2/\alpha_g$) was $t_{g,r} \sim (5\text{-}20) \times 10^{-3}$ s (using gas properties in the range 680 to 1180 K). The corresponding times for solid heat conduction, axial (L^2/α_{FeCr}) and radial [$(\delta/2)^2/\alpha_{FeCr} + \delta_c{}^2/\alpha_{ZrO2}$], were $t_{s,x} \sim (1.6\text{–}2.4) \times 10^3$ s and $t_{s,r} \sim (0.3\text{–}0.4) \times 10^{-3}$ s, respectively (using the solid properties of Table 2 in the provided temperature ranges). Since the equilibration of the gas required times at least as long as $t_{g,r}$, the significantly faster radial solid heat conduction could not be resolved within the gas-phase quasisteady assumption. Thus, a 1-D approach for the solid has been adopted. A step of 50 ms, sufficiently long for gas-phase equilibration, was used for time integration.

Governing Equations

For a quasisteady laminar channel-flow with hetero-/homogeneous reactions, the governing equations in cylindrical coordinates become:

Continuity:

$$\frac{\partial(\rho u)}{\partial x} + \frac{1}{r}\frac{\partial(r\rho v)}{\partial r} = 0 \tag{1}$$

Axial momentum:

$$\frac{\partial(\rho u u)}{\partial x} + \frac{1}{r}\frac{\partial(r\rho v u)}{\partial r} = -\frac{\partial p}{\partial x} + \frac{\partial}{\partial x}\left[2\mu\frac{\partial u}{\partial x} - \frac{2}{3}\mu\left(\frac{\partial u}{\partial x} + \frac{1}{r}\frac{\partial(rv)}{\partial r}\right)\right] + \frac{1}{r}\frac{\partial}{\partial r}\left[\mu r\left(\frac{\partial u}{\partial r} + \frac{\partial v}{\partial x}\right)\right] \tag{2}$$

Radial momentum:

$$\frac{\partial(\rho u v)}{\partial x}+\frac{1}{r}\frac{\partial(r\rho v v)}{\partial r}=-\frac{\partial p}{\partial r}+\frac{\partial}{\partial x}\left[\mu\left(\frac{\partial v}{\partial x}+\frac{\partial u}{\partial r}\right)\right]+\frac{\partial}{\partial r}\left[2\mu\frac{\partial v}{\partial r}-\frac{2}{3}\mu\left(\frac{\partial u}{\partial x}+\frac{1}{r}\frac{\partial(rv)}{\partial r}\right)\right]+\frac{2\mu}{r}\left(\frac{\partial v}{\partial r}-\frac{v}{r}\right) \tag{3}$$

Total enthalpy:

$$\frac{\partial(\rho u h)}{\partial x}+\frac{\partial(r\rho v h)}{\partial r}=\frac{\partial}{\partial x}\left(\lambda_g\frac{\partial T}{\partial x}-\rho\sum_{k=1}^{Kg}Y_k h_k V_{k,x}\right)+\frac{1}{r}\frac{\partial}{\partial r}\left(r\lambda_g\frac{\partial T}{\partial r}-r\rho\sum_{k=1}^{Kg}Y_k h_k V_{k,r}\right) \tag{4}$$

Gas-phase species:

$$\frac{\partial(\rho u Y_k)}{\partial x}+\frac{1}{r}\frac{\partial(r\rho v Y_k)}{\partial r}=-\frac{\partial}{\partial x}(\rho Y_k V_{k,x})-\frac{1}{r}\frac{\partial}{\partial r}(r\rho Y_k V_{k,r})+\dot{\omega}_k W_k,\quad k=1,..,K_g \tag{5}$$

Surface species coverage:

$$\frac{\partial\theta_m}{\partial t}=\sigma_m\frac{\dot{s}_m}{\Gamma}\qquad m=1,..,M_s \tag{6}$$

The left side of Eqs. (6) was not a true transient term and its inclusion merely facilitated convergence to steady state. The diffusion velocities were computed using mixture-average plus thermal diffusion for the light species (Kee et al., 1996a):

$$\vec{V}_k=-\left(\frac{D_{km}}{Y_k}\right)\nabla Y_k+\left(\frac{D_k^T}{\rho Y_k T}\right)\nabla T\qquad k=1,..,K_g \tag{7}$$

Finally, the ideal gas and caloric state laws were:

$$p=\frac{\rho RT}{\bar{W}}\ \text{and}\ h_k=h_k^{\circ}(T_{\circ})+\int_{T_o}^{T}c_{p,k}\,dT,\quad \text{with}\ h=\sum_{k=1}^{Kg}Y_k h_k\quad k=1,..,K_g \tag{8}$$

The time-dependent energy balance for the 1-D solid was:

$$\left[\rho_{\mathrm{FeCr}}\frac{\partial(c_{\mathrm{FeCr}}T_W)}{\partial t}-\lambda_{\mathrm{FeCr}}\frac{\partial^2 T_W}{\partial x^2}\right]\frac{\delta}{2}-\left[\dot{q}_{\mathrm{rad}}-\lambda_g\frac{\partial T}{\partial r}\bigg|_{r=r_h-}+B\sum_{k=1}^{Kg}(\dot{s}_k h_k W_k)_{r=r_h}\right]\left(\frac{2r_h}{2r_h+\delta/2}\right)=0 \tag{9}$$

The solid thickness in Eq. (9) corresponded to half of the FeCr-alloy ($\delta/2 = 25\,\mu m$) due to the consideration of adjacent channels. The thinner catalyst layer ($\delta_c = 4.6\,\mu m$) was neglected since its thermal conductivity and thermal inertia ($\rho_{ZrO2} c_{ZrO2} \delta_c$) were at least an order of magnitude lower than those of the FeCr-alloy, irrespective of temperature. For the FeCr-alloy, a temperature-dependent heat capacity was considered (see footnote (b) of Table 2); the thermal conductivity was taken constant at its 300 K value of 16 W/mK, given the lack of specific literature data and the weak temperature dependence of similar alloys (Touloukian et al., 1970). The net received radiant heat flux ($\dot{q}_{rad}$ in Eq. (9)) accounted for the radiation exchange of each differential cylindrical surface element with all other differential surface elements as well as with the channel entry and outlet, and was modeled by the net radiation method for diffuse-gray areas (Siegel and Howell, 1981). Details of the radiation model have been provided elsewhere (Karagiannidis et al., 2007). The emissivities of all differential channel elements were equal to $\varepsilon = 0.6$, while the inlet and the outlet sections were treated as black bodies ($\varepsilon = 1.0$). The radiation exchange temperatures for the entry and outlet were considered equal to the corresponding mean gas temperatures. It will be shown, however, that radiation effects were altogether minimal.

Boundary Conditions and Method of Solution

The gas-phase species interfacial boundary conditions were:

$$(\rho Y_k V_{k,r})_{r=r_h-} + B \dot{s}_k W_k = 0, \quad k = 1, .., K_g \tag{10}$$

with $\dot{s}_k = 0$ over the inactive channel length. The factor B in Eqs. (9) and (10) was the ratio of the active to the geometrical surface area and has been determined by H_2 chemisorption. Those tests provided the active areas in m^2/gr-Rh for the used catalysts; with known size, weight and noble metal content of the analyzed samples, the values of B could be calculated (see Table 1). It is noted that the fresh samples had considerably higher measured B factors as they comprised both high-surface-area tetragonal phase and low-surface-area monoclinic ZrO_2 phase (detected with surface Raman measurements), while the used samples comprised only monoclinic phase (Eriksson et al., 2006). The B values of the used samples were maintained in successive combustion runs and were, therefore, employed in the ensuing simulations (in all cases of Table 1 the catalysts had already been exposed to combustion environments at foregoing runs). Intraphase species diffusion was not considered since the catalyst layer was only 4.6 μm thick and was applied on a non-porous FeCr-alloy.

Radiative boundary conditions were applied at the reactor inlet and outlet:

$$\begin{aligned} \lambda_{FeCr} \frac{\partial T_W}{\partial x} &= \varepsilon\sigma[T_W^4(x) - T_{IN}^4] \quad \text{at } x = -L_u \\ -\lambda_{FeCr} \frac{\partial T_W}{\partial x} &= \varepsilon\sigma[T_W^4(x) - T_{OUT}^4] \quad \text{at } x = L_c + L_u \end{aligned} \tag{11}$$

Uniform profiles for the axial velocity, the species mass fractions and the temperature were specified at the inlet. The 8 mm gap between the flow straightener and the honeycomb entry created only a very thin boundary layer (less than 0.4 mm thick, since the Reynolds numbers in the 35 mm diameter holder tube exceeded 15,000), thus justifying the consideration of a single representative channel with a constant inlet velocity. Moreover, the adiabaticity of the honeycomb reactor was attested by the gas analysis and temperature measurements; the differences between the inlet and outlet total enthalpies corresponded to equivalent temperature differences of less than 15 K. It is worth mentioning that, apart from the good thermal insulation, the adiabaticity was aided by the particularly large (for laboratory-scale tests) honeycomb diameter (35 mm) that resulted in a low external surface-to-volume ratio. At the symmetry axis ($r = 0$) and the outlet ($x = L_c + L_u$) zero-Neumann boundary conditions were applied for all thermoscalars and the axial velocity, while the radial velocity was set to zero. Finally, no-slip conditions were used for both velocity components at $r = r_h$.

The coupled set of flow and solid equations (Eqs. (1) to (6) and Eq. (9)) were solved simultaneously. A finite volume scheme was adopted for the spatial discretization of the flow equations and solution was obtained with a SIMPLER method for the pressure-velocity field (Patankar, 1980); details on the quasi-steady flow solution have been provided elsewhere (Dogwiler et al., 1999; Mantzaras et al., 2000; Appel et al., 2002). For the transient solid equation, a second order accurate, fully implicit scheme was constructed by using a quadratic backward time discretization (Ferziger and Petric, 1999). At a given time step, the coupled flow and solid phases were solved iteratively such that at convergence the solid temperature did not vary by more than 10^{-4} K. An orthogonal staggered grid of 220×24 points in x and r, respectively, (75 mm $\times$ 0.6 mm) with finer axial spacing towards the start of the catalytic section and radial spacing closer to the wall, was sufficient to produce a grid-independent solution; the axial discretizations in the solid and gas were the same (220 points). For time integration, the step was $\Delta t = 50$ ms. Simulations of selected cases with steps of 35, 40 and 70 ms were in good agreement with the $\Delta t = 50$ ms results. The CPU time for a 10-sec-long integration was $\sim$15 h on a 2.6 GHz Opteron processor when gas chemistry was not included (otherwise the CPU time increased by a factor of 4). Finally, a cluster of twenty same processors was used for elaborate parametric studies.

Chemical Kinetics

The detailed catalytic scheme of Deutschmann (Schwiedernoch et al., 2003) has been employed (38 reactions, 12 surface and 6 gaseous species, see Table 3). Earlier kinetic studies have shown (Appel et al., 2005) that this scheme reproduced the measured methane conversion and synthesis gas yields in CPO of CH_4/air, at least over the reactor extent were oxygen was still available; in the experiments of Table 1, a small oxygen breakthrough was always assured. More recent kinetic studies (Schneider et al., 2007) have also attested the aptness of the catalytic scheme in CPO of methane with EGR at pressures of 4 to 10 bar.

For gas-phase chemistry, the C_2/H/O mechanism of Warnatz et al. (1996) was used (164 reversible reactions and 34 species). This mechanism has reproduced

Table 3 Heterogeneous reaction scheme[a]

	Adsorption reactions	$A(\gamma)$	b	E
S1.	$CH_4 + Rh(s) \rightarrow CH_4(s)$	0.008	0.0	0.0
S2.	$O_2 + 2Rh(s) \rightarrow 2O(s)$	0.01	0.0	0.0
S3.	$H_2 + 2Rh(s) \rightarrow 2H(s)$	0.01	0.0	0.0
S4.	$H_2O + Rh(s) \rightarrow H_2O(s)$	0.1	0.0	0.0
S5.	$CO_2 + Rh(s) \rightarrow CO_2(s)$	10^{-5}	0.0	0.0
S6.	$CO + Rh(s) \rightarrow CO(s)$	0.5	0.0	0.0
	Surface reactions			
S7.	$H(s) + O(s) \rightarrow OH(s) + Rh(s)$	5.0×10^{22}	0.0	83.7
S8.	$OH(s) + Rh(s) \rightarrow H(s) + O(s)$	3.0×10^{20}	0.0	37.7
S9.	$H(s) + OH(s) \rightarrow H_2O(s) + Rh(s)$	3.0×10^{20}	0.0	33.5
S10.	$H_2O(s) + Rh(s) \rightarrow H(s) + OH(s)$	5.0×10^{22}	0.0	106.4
S11.	$OH(s) + OH(s) \rightarrow H_2O(s) + O(s)$	3.0×10^{21}	0.0	100.8
S12.	$H_2O(s) + O(s) \rightarrow OH(s) + OH(s)$	3.0×10^{21}	0.0	224.2
S13.	$C(s) + O(s) \rightarrow CO(s) + Rh(s)$	3.0×10^{22}	0.0	97.9
S14.	$CO(s) + Rh(s) \rightarrow C(s) + O(s)$	2.5×10^{21}	0.0	169.0
S15.	$CO(s) + O(s) \rightarrow CO_2(s) + Rh(s)$	1.4×10^{20}	0.0	121.6
S16.	$CO_2(s) + Rh(s) \rightarrow CO(s) + O(s)$	3.0×10^{21}	0.0	115.3
S17.	$CH_4(s) + Rh(s) \rightarrow CH_3(s) + H(s)$	3.7×10^{21}	0.0	61.0
S18.	$CH_3(s) + H(s) \rightarrow CH_4(s) + Rh(s)$	3.7×10^{21}	0.0	51.0
S19.	$CH_3(s) + Rh(s) \rightarrow CH_2(s) + H(s)$	3.7×10^{24}	0.0	103.0
S20.	$CH_2(s) + H(s) \rightarrow CH_3(s) + Rh(s)$	3.7×10^{21}	0.0	44.0
S21.	$CH_2(s) + Rh(s) \rightarrow CH(s) + H(s)$	3.7×10^{24}	0.0	100.0
S22.	$CH(s) + H(s) \rightarrow CH_2(s) + Rh(s)$	3.7×10^{21}	0.0	68.0
S23.	$CH(s) + Rh(s) \rightarrow C(s) + H(s)$	3.7×10^{21}	0.0	21.0
S24.	$C(s) + H(s) \rightarrow CH(s) + Rh(s)$	3.7×10^{21}	0.0	172.8
S25.	$CH_4(s) + O(s) \rightarrow CH_3(s) + OH(s)$	1.7×10^{24}	0.0	80.3
S26.	$CH_3(s) + OH(s) \rightarrow CH_4(s) + O(s)$	3.7×10^{21}	0.0	24.3
S27.	$CH_3(s) + O(s) \rightarrow CH_2(s) + OH(s)$	3.7×10^{24}	0.0	120.3
S28.	$CH_2(s) + OH(s) \rightarrow CH_3(s) + O(s)$	3.7×10^{21}	0.0	15.1
S29.	$CH_2(s) + O(s) \rightarrow CH(s) + OH(s)$	3.7×10^{24}	0.0	158.4
S30.	$CH(s) + OH(s) \rightarrow CH_2(s) + O(s)$	3.7×10^{21}	0.0	36.8
S31.	$CH(s) + O(s) \rightarrow C(s) + OH(s)$	3.7×10^{21}	0.0	30.1
S32.	$C(s) + OH(s) \rightarrow CH(s) + O(s)$	3.7×10^{21}	0.0	145.5
	Desorption reactions			
S33.	$2H(s) \rightarrow H_2 + 2Rh(s)$	3.0×10^{21}	0.0	77.8
S34.	$2O(s) \rightarrow O_2 + 2Rh(s)$	1.3×10^{22}	0.0	$355.2–280\theta_O$
S35.	$H_2O(s) \rightarrow H_2O + Rh(s)$	3.0×10^{13}	0.0	45.0
S36.	$CO(s) \rightarrow CO + Rh(s)$	3.5×10^{13}	0.0	$133.4\text{-}15\theta_{CO}$
S37.	$CO_2(s) \rightarrow CO_2 + Rh(s)$	1.0×10^{13}	0.0	21.7
S38.	$CH_4(s) \rightarrow CH_4 + Rh(s)$	1.0×10^{13}	0.0	25.1

[a]From Schwiedernoch et al. (2003). The reaction rate coefficient is $k = AT^b exp(-E/RT)$, A (mol-cm-sec) and E (kJ/mol). In the adsorption reactions, A denotes a sticking coefficient (γ). The suffix (s) designates a surface species. The surface site density is $\Gamma = 2.72 \times 10^{-9}$mol/cm^2.

homogeneous ignition characteristics in the aforementioned CPO studies without and with EGR (Appel et al., 2005; Schneider et al., 2007). Selected simulations have shown that, for the present moderate pressures, the homogeneous reaction pathway was negligible not only during the transient light-off event but also during the steady operation where the surface temperatures were the highest (for the latter, see also

discussion in Schneider et al. (2006)). Gas phase chemistry was also negligible over the 45-mm-long gap separating the reactor exit and the sampling probe (Figure 1a), as shown by additional steady plug-flow reactor simulations. The minimal impact of gaseous chemistry was also demonstrated experimentally: when the cooling water of the sampling probe was turned off, the relative increase in the measured hydrogen composition was only 3%, despite the fact that the residence time in the visibly-hot part of the probe was about 10 times longer than that of the reactor.

Transport properties were evaluated using the CHEMKIN database (Kee et al., 1996a). Gas-phase thermodynamic data were included in the provided scheme (Warnatz et al., 1996). Finally, surface and gas-phase reaction rates (the latter were excluded from the ensuing computations) were evaluated with SURFACE CHEMKIN (Coltrin et al., 1996) and CHEMKIN (Kee et al., 1996b), respectively.

Ideal Reactor Modeling

To decouple the underlying chemical processes from reactor effects (e.g., properties of solid) additional computations have been carried out with ideal reactor models. Ignition delay times were computed in a constant pressure batch reactor. For this purpose, the homogeneous-reaction package SENKIN of CHEMKIN (Lutz et al., 1996) has been extended to include catalytic reactions. The governing equations were as follows:

Gas-phase species equation:

$$\rho \frac{dY_k}{dt} = \left(\dot{\omega}_k + \frac{S}{V} \dot{s}_k \right) W_k \quad k = 1, .., K_g \tag{12}$$

Energy equation:

$$c_p \frac{dT}{dt} = -\frac{1}{\rho} \left[\sum_{k=1}^{Kg} h_k \dot{\omega}_k W_k + \frac{S}{V} \sum_{k=1}^{Kg+Ms} h_k \dot{s}_k W_k \right] \tag{13}$$

with S and V the reactor surface and volume, respectively. Equations (12), (13) and (6), supplemented by the gas laws of Eq. (8), were solved subject to appropriate initial conditions.

Finally, the surface perfectly stirred reactor (SPSR) package of CHEMKIN (Moffat et al. 1993) facilitated the ignition/extinction studies:

Gas-phase species equations:

$$\frac{dY_k}{dt} = -\frac{1}{\tau} (Y_k - Y_{k,\mathrm{IN}}) + \frac{1}{\rho} \left(\dot{\omega}_k + \frac{S}{V} \dot{s}_k \right) W_k \quad k = 1, .., K_g \tag{14}$$

Energy equation:

$$c_p \frac{dT}{dt} = \frac{1}{\tau} \sum_{k=1}^{Kg} Y_{k,\mathrm{IN}} (h_k - h_{k,\mathrm{IN}}) - \frac{1}{\rho} \left[\sum_{k=1}^{Kg} h_k \dot{\omega}_k W_k + \frac{S}{V} \sum_{k=1}^{Kg+Ms} h_k \dot{s}_k W_k \right] \tag{15}$$

with τ the reactor residence time. The surface coverage and gas laws were given by Eqs. (6) and (8), respectively.

RESULTS AND DISCUSSION

Catalytic Ignition

Measured and predicted temporal profiles of temperature are provided in Figure 2 for Case 1; predictions are shown for both the surface and the mean (radially averaged) gas temperatures. Computed axial surface temperature profiles at selected time intervals are further given in Figure 3. During the ramping of the inlet temperature in the experiments, a small catalytic reactivity was always present for $T_{IN} > 600\,K$, which resulted in measured reactor temperatures slightly higher than the corresponding T_{IN}. For consistency with the experiments, the initial solid temperature in the numerical model ($t = 0$ in Figures 2 and 3) has been obtained by solving first a transient case at a lower inlet temperature ($T_{IN} = 670\,K$) up to the time that yielded surface temperatures close to the measurements. It is, nonetheless, clarified that the small initial temperature excursions above $T_{IN} = 680\,K$ (less

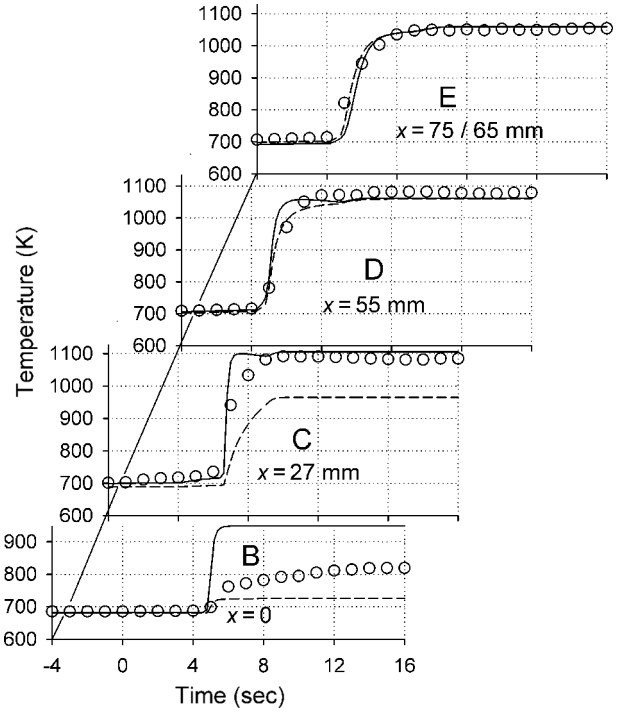

Figure 2 Predicted (lines) and measured (symbols) temperatures at axial positions *B* through *E* for Case 1. Predictions are given for the wall temperature (solid lines) and the mean gas temperature (dashed lines). At position *E*, the measurements refer to the mean gas temperature 10 mm downstream of the reactor ($x = 75\,mm$), while the predictions refer to the mean gas temperature at the reactor exit ($x = 65\,mm$).

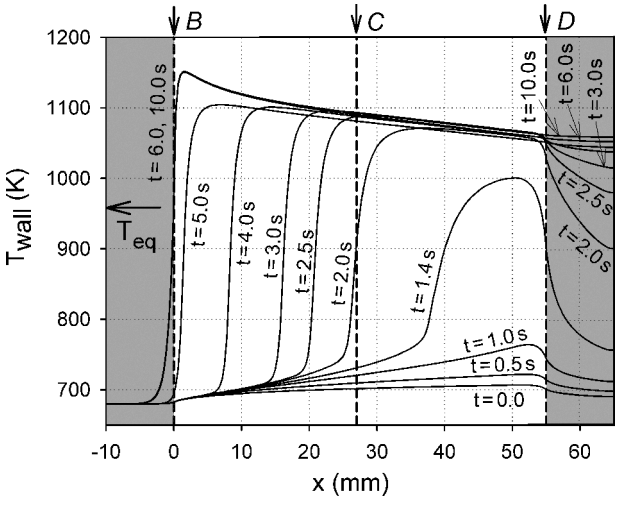

Figure 3 Predicted axial profiles of wall temperature at different times for Case 1. The shaded areas denote the non-catalytic part of the reactor. The vertical arrows at *B*, *C* and *D* indicate the thermocouple locations inside the reactor. The horizontal arrow marked T_{eq} denotes the adiabatic equilibrium temperature.

than 25 K at $t = 0$, as shown in Figures 2 and 3) had a minimal impact on the subsequent time evolution of the ignition event.

The predictions reproduced well, at all 4 positions, the measured elapsed times for the onset of sharp temperature rise, the temporal extent of the main transient event, and also the final temperatures. At position *E*, the relevant predictions of Figure 2 referred to the reactor exit ($x = 65$ mm); therein the channel walls were inert, leading to predicted mean gas temperatures higher than the corresponding surface temperatures during the period of sharp temperature rise. The measured temperatures at the late ignition stages ($t \geq 10$ s), where steady-state has been practically reached, were in good agreement with the predicted surface temperatures (Figure 2). An exception was location *B*, with measurements in-between the predicted surface and mean gas temperatures. However, this can be attributed to the very steep spatial temperature gradients at position *B* (see Figure 3): an effective repositioning of thermocouple *B* at $x = -0.3$ mm could readily account for those differences. It is further noted that computations with $T_{IN} \leq 670$ K did not yield light-off (in the sense of a vigorous burning solution) for an integration period of up to 20 s, which was roughly threefold longer than the experimentally measured time needed to reach the steady-state wall temperature at $x = 0$ (see Figures 2 and 3). This outcome was in good agreement with the experimentally assessed inlet temperature for ignition ($T_{IN} = 680$ K).

To facilitate the ensuing discussion, the main reaction pathways are summarized by the following global steps:

$$CH_4 + 2O_2 = CO_2 + 2H_2O \quad \text{(total oxidation)} \tag{R1}$$

$$2CH_4 + O_2 = 2CO + 4H_2 \quad \text{(partial oxidation)} \tag{R2}$$

$$CH_4 + H_2O = CO + 3H_2 \quad \text{(steam reforming)} \tag{R3}$$

$$CO + H_2O = CO_2 + H_2 \text{(water gas shift)} \tag{R4}$$

$$CH_4 + CO_2 = 2CO + 2H_2 \quad (CO_2 \text{ reforming}) \tag{R5}$$

Mass rather than molar fractions will be preferably used thereafter, due to the presence of strongly non-equimolar reactions (R2, R3 and R5). The underlying chemical processes are discussed with the aid of Figures 4 and 5 that provide, at 3 selected times, the 2-D maps of temperature and major species mass fractions, and the species net production rates and selected production rate ratios, respectively. Ignition was initiated at the rear of the channel as shown in Figures 3 and 4(a).

Total oxidation of methane dominated at early times as manifested by the sharp rise of H_2O, CO_2 and temperature in Figure 4a and by the ~ 0.5 value of the CH_4:O_2 molar consumption ratio at the far upstream location of the reaction zone (see Figure 5(a) at $x \approx 36$ mm). H_2 and CO were not produced for $t < 1$ s, whereas at later times CO production commenced before that of H_2. At $t = 1.4$ s, both partial oxidation products were produced (Figure 5a), giving rise to the observed very low levels of H_2 and CO in Figure 4a. Following ignition, the reaction zone propagated upstream (Figure 3) with an accompanying increase in peak surface

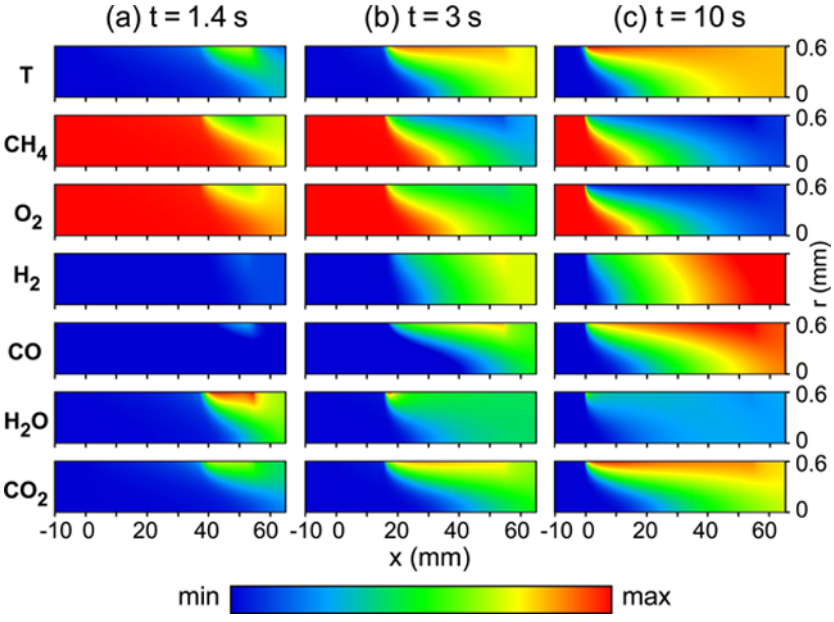

Figure 4 Predicted 2-D distributions of temperature and species mass fractions for Case 1 at three times: (a) 1.4 s, (b) 3.0 s, and (c) 10.0 s. The maximum and minimum levels of the color bar are: T: 681 K to 1146 K, CH_4: 0.039 to 0.131, O_2: 0.0 to 0.131, H_2: 0.0 to 0.0186, CO: 0.0 to 0.123, H_2O: 0.332 to 0.398, and CO_2: 0.406 to 0.478. The centerline is at $r = 0$ and the gas-solid interface at $r = 0.6$ mm. The catalytically active part of the reactor extents over $0 \leq x \leq 55$ mm.

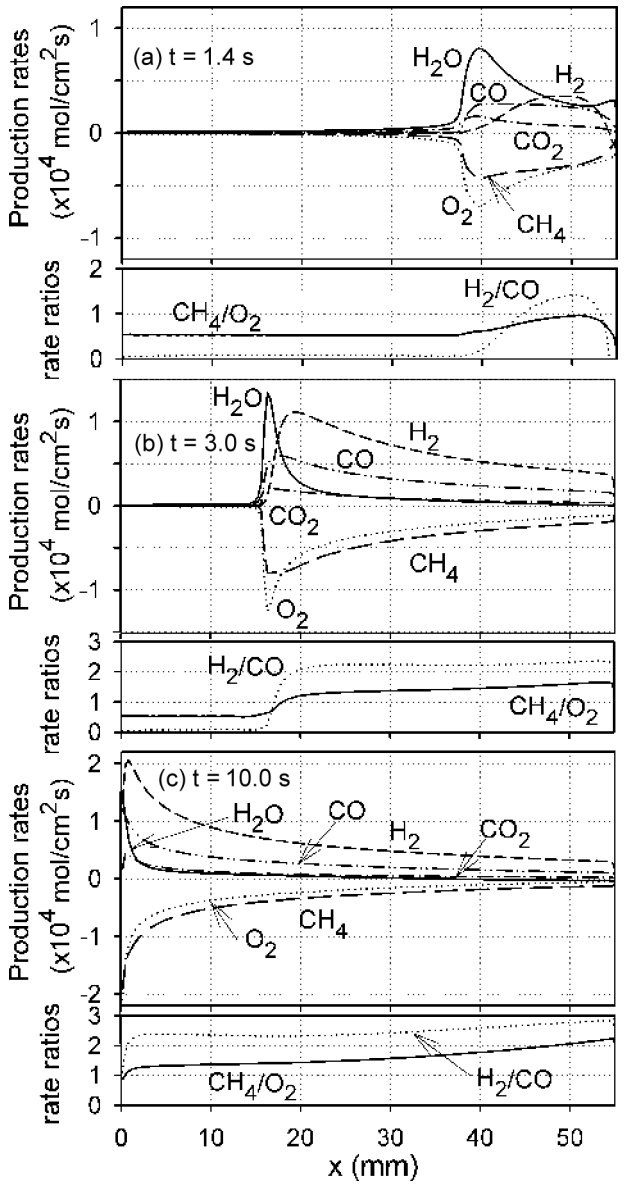

Figure 5 Computed axial profiles (Case 1) of species molar production rates (solid lines: H_2O, short dashed lines: H_2, double-dotted-dashed lines: CO, dotted-dashed lines: CO_2, long dashed lines: CH_4, dotted lines: O_2) and production rate-ratios (solid lines: CH_4:O_2, dotted lines: H_2/CO) at 3 times: (a) 1.4 s, (b) 3.0 s, and (c) 10.0 s.

temperature due to the gradual heat-up of the wall and the diminishing accumulation of heat in the solid mass. The peak temperature reached the front of the catalytically coated section at $t \approx 6$ s, while at $t \approx 10$ s steady-state had been practically achieved over the entire reactor length (Figure 3). The wall and mean gas temperatures exceeded

by as much as $\sim 200\,\mathrm{K}$ the adiabatic equilibrium temperature ($T_{eq} = 959\,\mathrm{K}$, see Figures 2 and 3), a condition typical in CPO reactors with residence times of a few milliseconds (Veser and Frauhammer, 2000; Schneider et al., 2006).

The approach to steady state is also illustrated in Figure 6a, providing the predicted mean (radially averaged) outlet species mass fractions versus time (black lines) and the corresponding GC steady-state measurements (the latter obtained at $t > 5\,\mathrm{min}$). The agreement between the measured and predicted outlet compositions was particularly good for all species; using the measured outlet species mass fractions and temperature, the calculated total enthalpy was within 0.4% of the corresponding inlet value (which was equivalent to a temperature differential of 15 K) and the C/H/O element balances were within 0.5%. For $t > 1.6\,\mathrm{s}$, H_2 and CO were formed at the upstream locations of the reaction zone mainly by the CPO reaction (R2) as manifested by the $\sim$2:1 production ratio of H_2:CO (Figures 5b, 5c). It is clarified that, as time progressed, the CO and H_2 formed increasingly closer to the front of

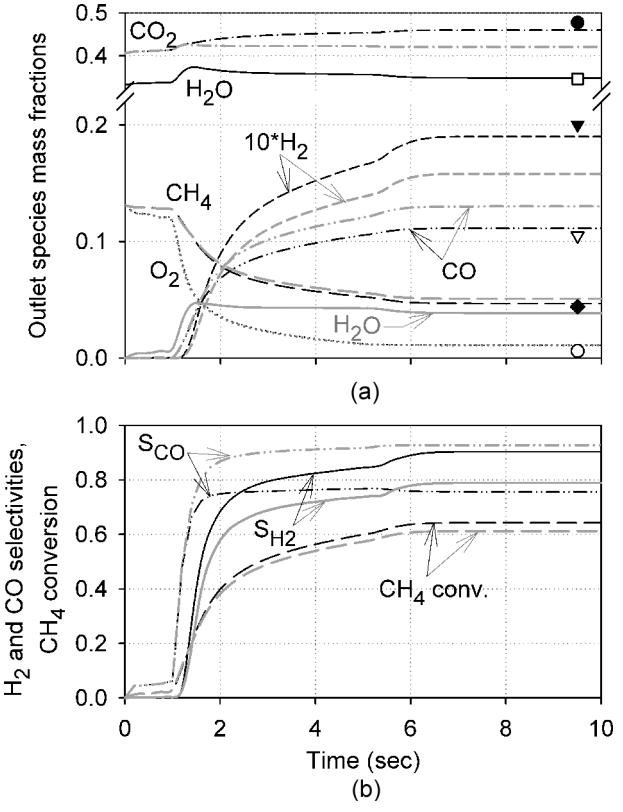

Figure 6 a. Predicted mean species mass fractions at the reactor outlet ($x = 65\,\mathrm{mm}$) versus time. Black lines: Case 1, gray lines: conditions same as in Case 1 with the inlet 46.3% H_2O replaced by equal amount of chemically inert H_2O^*. The symbols denote the steady state GC measurements (CO_2: filled circle, H_2O: open square, $10xH_2$: filled triangle, CO: open triangle, CH_4: filled diamond, O_2: open circle). 6b. Predicted selectivities for H_2 and CO and fractional CH_4 conversion (the notation of the black and gray lines is the same as in 6a).

the reaction zone. As in matter of fact, for $t > 2\,s$ both total and partial oxidation products were formed at the reaction zone front. This is illustrated by the CH_4:O_2 ratios in Figures 5b and 5c, which increased at the tip of the reaction zone from 0.55 ($t = 3\,s$) to 0.88 ($t = 10\,s$) indicating the growing contribution of the CPO reaction. This behavior was differentiated from earlier CH_4/air CPO studies without EGR (Schwiedernoch et al., 2003), whereby only total oxidation has been reported at the upstream reactor positions.

As the temperature of the catalyst increased, H_2 and CO were also produced farther downstream by the slower endothermic steam reforming (R3); this was manifested by the corresponding streamwise increase in the H_2:CO production ratio to values above 2.0 (Figures 5b and 5c) and by the corresponding drop in surface temperature (Figure 3). The surface temperatures had reached high enough levels for appreciable steam reforming, particularly at $t > 5.2\,s$, as seen by the sudden increase (decrease) in the H_2 (H_2O) profile of Figure 6a. At $t > 6\,s$, water gas shift (R4) started playing a modest role at the far downstream positions: this was evidenced by the continuing small production of CO_2 and the corresponding rise of the H_2:CO ratio at the far end of the active channel section ($x > 50\,mm$, Figure 5c). Therein, the O_2 consumption rates were too low to justify production of CO_2 via the oxidation route R1. On the other hand, the water gas shift reaction was found to be altogether insignificant in CH_4/air CPO without EGR (Schwiedernoch et al., 2003). It is finally noted that at all times there was always a small amount of O_2 breakthrough at the reactor exit (Figure 6).

The surface coverage for Case 1 is provided in Figure 7 at two selected times. The main coverage at early times, where the temperature was low, was O(s) (Figure 7a). The presence of O(s) inhibited ignition because high enough surface temperatures were required to shift the adsorption/desorption equilibria of O_2 towards desorption and thus release free surface sites for methane to adsorb. Although the mechanism of O(s) inhibition in catalytic ignition was the same for either fuel-lean or fuel-rich conditions (Deutschmann et al., 1996; Dogwiler et al., 1999; Schwiedernoch et al., 2003; Schneider et al., 2006), it was less pronounced in the latter due to the lower O_2 content. Upon ignition, CO(s) and free sites (Rh(s)) became the dominant surface coverage. The partial oxidation product selectivities, defined as:

$$S_{H2} = \frac{0.5\,Y_{H2}/W_{H2}}{(Y_{CH4,IN} - Y_{CH4,OUT})/W_{CH4}}$$

and

$$S_{CO} = \frac{Y_{CO}/W_{CO}}{(Y_{CH4,IN} - Y_{CH4,OUT})/W_{CH4}} \tag{16}$$

along with the fractional methane conversion at the reactor outlet are provided in Figure 6b (black lines). The definition of S_{H2} in Eq. (16) was based on the stoichiometry of the CPO reaction and has been maintained herein, despite the added H_2 production from H_2O. At steady state, $S_{H2} = 0.91$ and $S_{CO} = 0.74$ while the methane conversion was 64%.

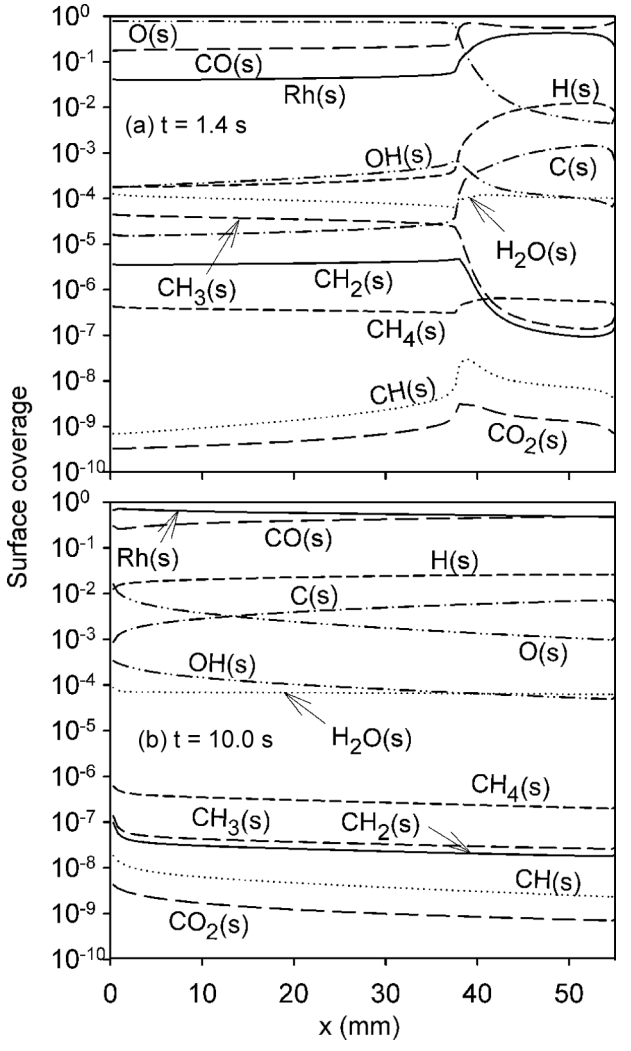

Figure 7 Surface coverage for Case 1 at two times: (a) 1.4 s and (b) 10 s.

Impact of H_2O and CO_2 Dilution on Catalytic Ignition

Despite the added large amount of CO_2, the contribution of dry (CO_2) reforming was negligible as also shown in our previous steady-state investigation (Schneider et al., 2006). The reason was that oxy- and H_2O-reforming reactions were considerably faster than dry reforming (Mark and Maier, 1996) and the dominance of the former steps was further accentuated by the present short contact times. The absence of dry reforming has also been attested in CH_4/air CPO without EGR (Veser and Frauhammer, 2000; Schwiedernoch et al., 2003).

To investigate the impact of water on the synthesis gas yields and selectivities, additional predictions have been carried out for Case 1, whereby the 46.3% H_2O

feed content was replaced by a fictitious species H_2O^* that had the same thermodynamic and transport properties as H_2O but did not participate in any reaction. H_2O^* simulated only the incoming steam whereas the catalytic pathway was still allowed to create combustion-generated H_2O. Computations with H_2O^* and normal H_2O dilution are compared in Figures 6 and 8. It is evident that the presence of water increased (decreased) the H_2 (CO) selectivity and slightly enhanced the methane conversion (Figure 6b), while it moderated somewhat the surface temperatures (Figure 8). This was because H_2O provided a source of surface O(s) and OH(s) radicals that facilitated the steps S33 and S15 against S7/S9 and S36 (see Table 3), respectively, as has been elaborated in earlier steady CPO studies (Schneider et al., 2006).

The comparison between the black and gray H_2O lines in Figure 6a further indicated that the added amount of H_2O facilitated steam reforming mainly by depleting faster the water produced by total oxidation (R1) rather than by consuming the incoming steam itself (at any time, $Y_{H2O,OUT}(t) > Y_{H2O,IN}$ in Figures 6a and 4). This was because the surface temperatures were moderate and the residence times too short for the slow endothermic steam reforming to dominate. Of importance in the present transient analysis, was that the chemical impact of water was already evidenced at early times (e.g., $t > 1.5$ s) as seen in Figure 6. However, the effect of added water grew to larger importance at later times when a significant extent of the channel attained high temperatures.

Despite the chemical impact of H_2O and the associated somewhat lower surface temperatures (by as much as 26 K compared to the H_2O^* dilution, see Figure 8) due to the enhanced impact of steam reforming, the times required for the onset of ignition and for the propagation of the reaction zone to the front of the catalytic section ($x = 0$) were practically the same in both H_2O and H_2O^* dilution (Figure 8). To isolate reactor parameters (heat conduction in the solid, etc.) from chemical

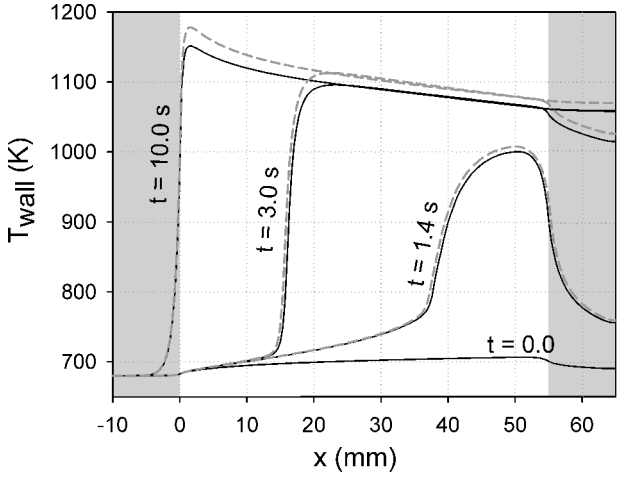

Figure 8 Predicted axial profiles of wall temperature at different times. Solid black lines: Case 1, dashed gray lines: conditions same as Case 1 with the inlet 46.3% H_2O replaced by equal amount of chemically inert H_2O^*. The shaded areas denote the non-catalytic part of the reactor.

effects, ignition delay times have been computed in a batch reactor (Eqs. (12) and (13), with only surface reactions included) using $S/V = 33.3\,cm^{-1}$, so as to mimic the confinement of the channel experiments. The catalytic ignition delay times, τ_{ig}, (defined as the times required to reach the 50% rise between inlet and final temperatures) were practically independent of dilution type (15.2 ms for the H_2O and 15.0 ms for the H_2O^*). The reason for this rather unexpected behavior is illustrated in Figure 9, providing the normalized sensitivity coefficients of the ignition delay time $[=(A_i/\tau_{ig})\ (\partial\tau_{ig}/\partial A_i)$, with A_i the pre-exponential of the i-th reaction] for the eight most significant reactions of Table 3.

The dominant reaction controlling catalytic ignition (in either H_2O or H_2O^* dilution) was S15, the surface oxidation of CO(s) to CO_2(s). Upon ignition, CO(s) and free sites (Rh(s)) comprised the main surface coverage (see Figure 7). Before ignition, the high O(s) coverage reduced the amount of available free sites and hence inhibited ignition. An acceleration of S15 led to lower O(s), thus promoting ignition. It is nonetheless, instructive to consider not only the chemical but also the thermal impact of S15. This reaction eventually led to the formation of CO_2, the oxidation $CO \rightarrow CO_2$ being a main exothermic heat release step. The oxidation of H_2 to H_2O was less important, since the CO:H_2 molar ratio over the entire induction zone was at least ten. Catalytic ignition delay times were, therefore, dominated by total oxidation reactions forming CO_2, and as such they were not critically affected by reactions forming partial oxidation products (R2 and R4). In summary, the chemical impact of H_2O dilution, although important during the time evolution of the light-off event, was minimal on the ignition delay times themselves. This behavior was particular useful for gas-turbine CPO, which has stringent light-off temperature requirements.

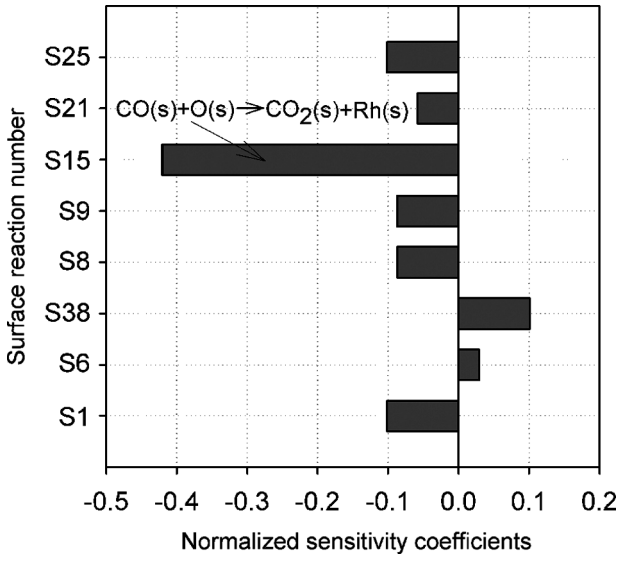

Figure 9 Normalized sensitivity coefficients for the 8 more sensitive surface reactions on the ignition delay time (Case 1). The reaction numbering follows Table 3.

Effect of Solid Properties on Catalytic Ignition

To complete the picture of the in-channel processes, the heat balance in the solid is shown in Figure 10. The heat generation ($\dot{q}_{gen}$) peaked nearly at the front of the reaction zone due to total oxidation. Radiation was altogether negligible, with only a minor net radiative heat transfer in the regions close to the front of the reaction zone. Repeating the computations with channel surfaces having $\varepsilon = 0$ or 1

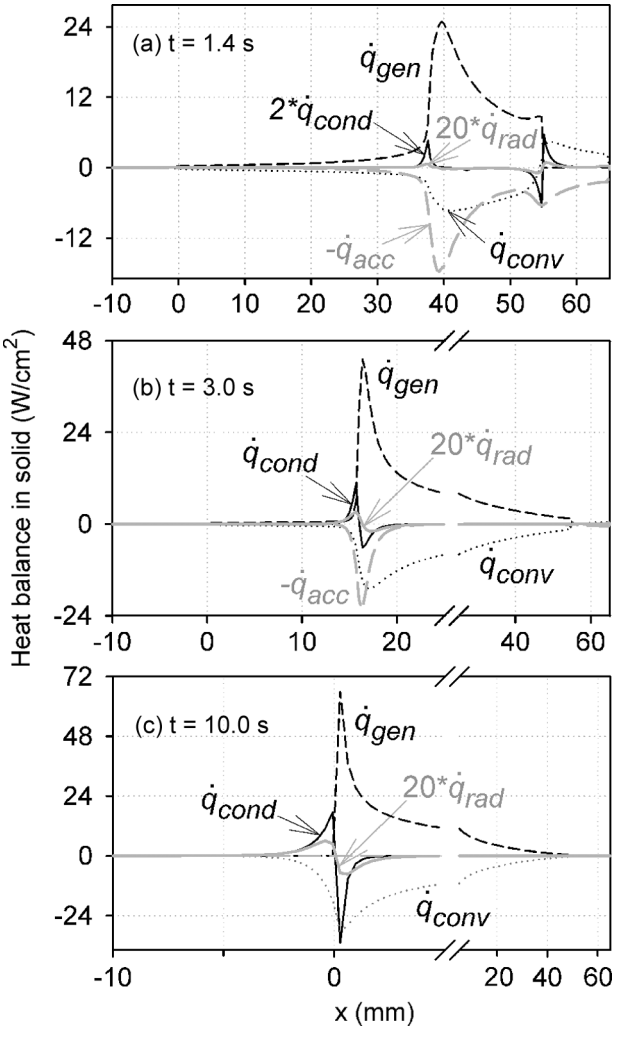

Figure 10 Heat balance in the solid for Case 1 at 3 times: (a) 1.4 s, (b) 3.0 s and (c) 10.0 s. Surface heat generation ($\dot{q}_{gen}$): dashed black lines; Convection ($\dot{q}_{conv}$): dotted black lines; Conduction ($\dot{q}_{cond}$): solid black lines; Radiation ($\dot{q}_{rad}$): solid gray lines, Negative of heat accumulation ($-\dot{q}_{acc}$): dashed gray lines. For clarity, $\dot{q}_{rad}$ has been expanded by a factor of 20, whereas $\dot{q}_{cond}$ has been expanded in (a) by a factor of two. The term $\dot{q}_{acc}$ is practically zero in (c).

reproduced essentially the same results. The negligible impact of $\dot{q}_{\text{rad}}$, even at steady-state operation where the surface temperatures were the highest, was a direct consequence of the diminished light-off distance that yielded wall temperatures at $t > 6$ s differing by less than 92 K over the extent $0 \leq x \leq 65$ mm (see Figure 3). On the other hand, in fuel-lean applications the more effective blocking of the surface free sites by oxygen (Dogwiler et al., 1999; Karagiannidis et al., 2007) could lead to appreciable temperature differences along the solid wall (>500 K); therein radiation exchange played an important role by transferring heat from the hotter rear channel surfaces to the colder entry, thus stabilizing combustion (Karagiannidis et al., 2007). Heat conduction ($\dot{q}_{\text{cond}}$) was more important at later times when steeper spatial temperature gradients formed at the front of the reaction zone (Figures 10b and 10c). Finally, heat accumulation had a dominant contribution at $t < 3$ s, while convection ($\dot{q}_{\text{conv}}$) transferred heat at early times from the gas to the rear channel solid inert section (Figure 10a).

The impact of solid properties on the light-off has also been investigated. Increasing or decreasing the solid thermal conductivity by a factor of two did not impact the time required for the onset of ignition. The elapsed times for the rear of the solid wall to heat up by 50 K or 300 K were roughly the same, as they were primarily controlled by chemical reactivity. On the other hand, the total upstream propagation time of the reaction zone decreased with increasing thermal conductivity although not linearly due to the continuing contribution of surface reactivity in the propagation speed (e.g., the total propagation time decreased from $\sim$6 s to $\sim$4.9 s when $\lambda = 32$ W/mK, and increased to $\sim$7.4 s when $\lambda = 8$ W/mK). In practical systems, where external heat losses may also be present, higher thermal conductivities are desirable. A similar investigation has shown a stronger impact of the solid specific heat (e.g., the total propagation time decreased from $\sim$5.8 s to $\sim$2.2 s when the specific heat decreased from 700 to 350 J/kgK, while it increased to $\sim$12.9 s for a specific heat of 1400 J/kgK). Although thermal conductivity and heat capacity were not the only factors considered in the selection of a CPO reactor material, the high thermal conductivity of metals (an order of magnitude larger than that of ceramics) was one of their main advantages.

Effect of Equivalence Ratio and Catalyst Loading on Catalytic Ignition

The catalytic ignition for Cases 6 and 10 is presented next, emphasizing mainly on their differences with Case 1. The Rh loading has been halved in Case 6, resulting in increased preheat requirements, with ignition attained at $T_{\text{IN}} = 730$ K. The predicted temperatures were, at all four monitoring locations, in good agreement with the measurements in terms of elapsed times for the arrival of the reaction zone and final temperatures (see Figure 11). The overall duration of the light-off event was, nevertheless, considerably shorter compared to Case 1 ($\sim$3 s, see Figure 12). Of interest in Case 6 was the particular mode of reaction zone propagation. Contrary to Case 1, where the reaction front propagated upstream (Figure 3), in Case 6 the reaction zone spread over most of the channel active section ($0 \leq x \leq 55$ mm) shortly after ignition ($t \sim 0.4$ s). At later times the surface temperatures increased over the entire active reactor length, as the heat accumulation in the solid diminished (plots

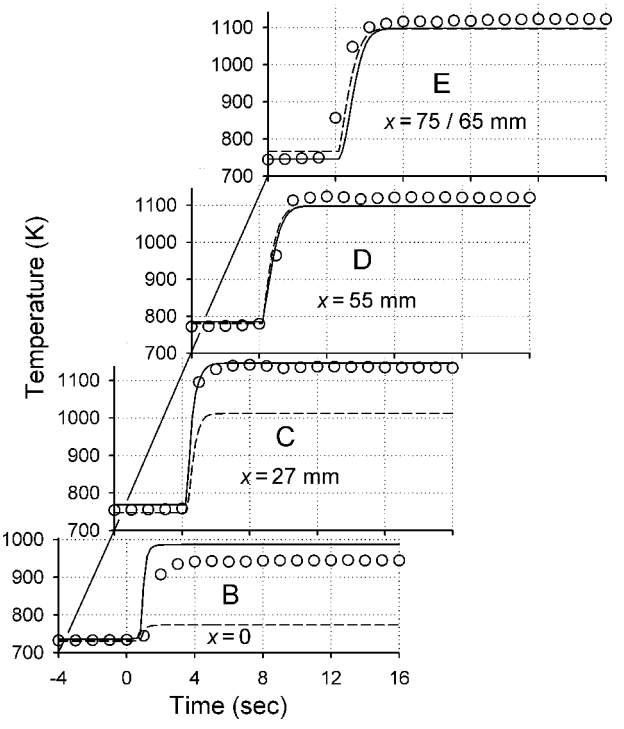

Figure 11 Predicted (lines) and measured (symbols) temperatures at axial positions *B* through *E* for Case 6. Predictions are provided for the wall temperature (solid lines) and mean gas temperature (dashed lines). At position *E*, the measurements refer to the mean gas temperature 10 mm downstream of the reactor exit (x = 75 mm), while the predictions refer to the reactor exit (x = 65 mm).

similar to that of Figure 10 revealed that $\dot{q}_{\mathrm{acc}}$ became insignificant after 1.3 s). Therefore, light-off was mainly controlled by the surface reactivity and the solid thermal inertia ($\rho_{\mathrm{ZrO2}} c_{\mathrm{ZrO2}} \delta_c$), with the solid thermal conductivity playing a secondary role. Further simulations indicated that light-off could not be achieved for $T_{\mathrm{IN}} \leq 710$ K over an integration period of 5 sec (about threefold longer than the time needed in the experiments to reach the steady wall temperature at $x \approx 0$, see Figures 11 and 12); this result was in fair agreement with the measured light-off temperature $\mathrm{T_{IN}} = 730$ K. It is finally worth mentioning that the only model parameter needed to capture the effect of catalyst loading was *B* (Eqs. (9), (10)), which was not arbitrarily adjusted but determined experimentally.

Equivalence ratios of 3.5 to 4.0 were optimal for CPO in chemical industry. In power generation applications, however, the use of even lower fuel-rich stoichiometries may be beneficial. It can be shown that, when using lower ϕ the CPO outlet temperatures and compositions yield enhanced gas-phase reactivity that, in turn, aids the stability of the follow-up homogeneous combustion zone; details on the gas-phase reactivity of the CPO products are outside the scope of the present work. Figure 13 provides comparisons between predicted and measured temperatures versus time for Case 10 ($\varphi = 2.5$). The propagation mode of the reaction zone

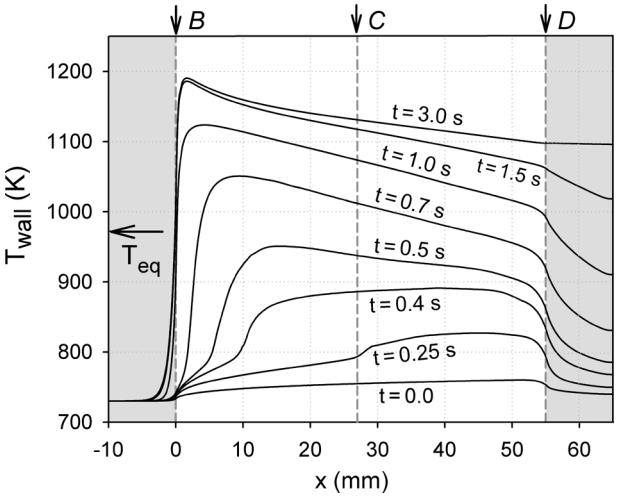

Figure 12 Predicted axial profiles of the wall temperature at different times for Case 6. The shaded areas denote the non-catalytic part of the reactor. The vertical arrows at *B*, *C* and *D* indicate the thermocouple locations inside the reactor, while the horizontal arrow marked T_{eq} denotes the adiabatic equilibrium temperature.

resembled that of Case 6 (Figure 12) and is not shown herein. As discussed in the previous section, the larger oxygen content inhibited catalytic ignition and this was evidenced by the higher (compared to Case 1) required inlet temperature ($T_{IN} = 725\,K$). The agreement between measurements and predictions in Figure 13 was fair, however, the elapsed times for reaction zone arrival were underpredicted and the peak temperatures were overpredicted.

Also seen in the comparisons of steady-state species mass fractions in Figure 14, the catalytic reaction scheme overpredicted (underpredicted) the H_2 (H_2O) levels. Moreover, it underpredicted (overpredicted) to an even greater extent the CO (CO_2) levels, suggesting a stronger surface oxidation of CO to CO_2. Those differences could be attributed to the fact that the surface scheme has been validated for equivalence ratios between 3.5 to 4.0 (Schwiedernoch et al., 2003) which are optimal for chemical synthesis, and extension to lower φ cannot be warranted. Despite the aforementioned discrepancies between measurements and predictions, the measured H_2 and CO yields were still high due to the elevated surface temperatures (the measured temperatures in Case 10 were up to 1250 K, i.e., $\sim$150 K higher than those of Case 1, see Figures 2 and 13). Such high temperatures could still be tolerated by the catalyst and the FeCr-alloy structure, suggesting that operation at φ as low as 2.5 could be attractive for gas turbines with EGR. The disadvantage of higher preheat with decreasing φ could be alleviated by increasing the Rh loading, as discussed in the foregoing comparisons of Cases 1 and 6. It is finally clarified that in CH_4/air CPO without EGR, φ as low as 2.5 could endanger the catalyst/reactor integrity (Appel et al., 2005) due the absence of large heat capacity gases (CO_2, H_2O) that moderate the reactor temperature.

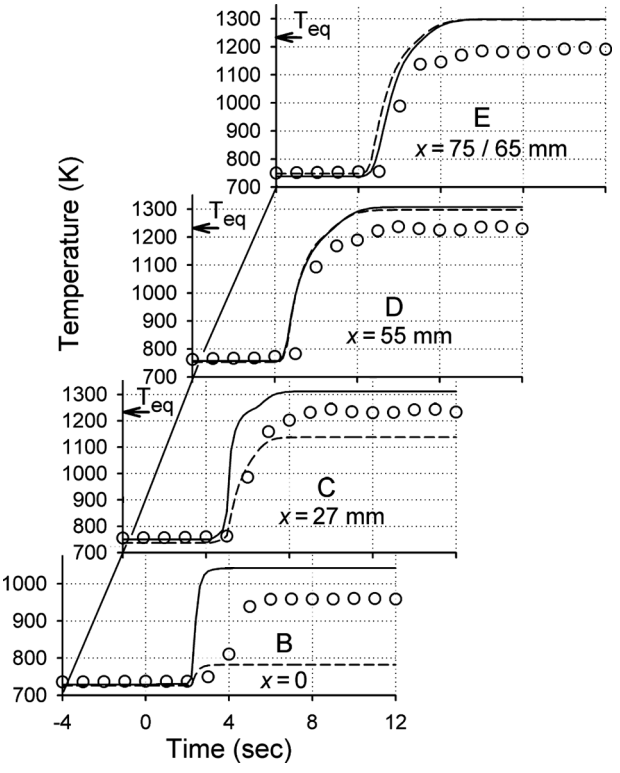

Figure 13 Predicted (lines) and measured (symbols) temperatures at the axial positions *B* through *E* for Case 10. Predictions are provided for the wall temperature (solid lines) and mean gas temperature (dashed lines). The horizontal arrows marked T_{eq} denote the adiabatic equilibrium temperature.

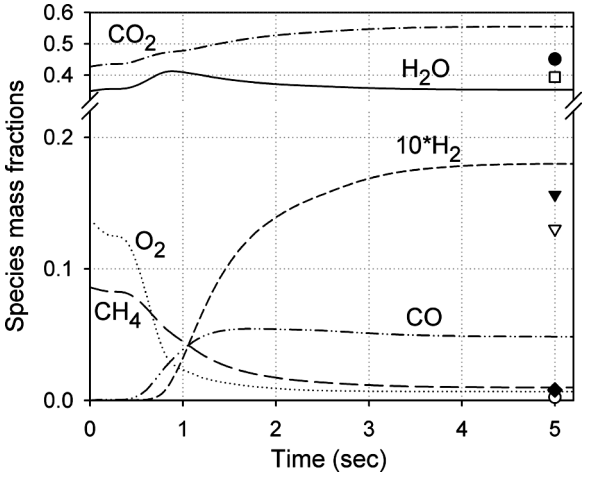

Figure 14 Predicted mean species mass fractions at the reactor outlet ($x = 65$ mm) versus time for Case 10. The symbols denote the steady state GC measurements (CO_2: filled circle, H_2O: open square, $10xH_2$: filled triangle, CO: open triangle, CH_4: filled diamond, O_2: open circle).

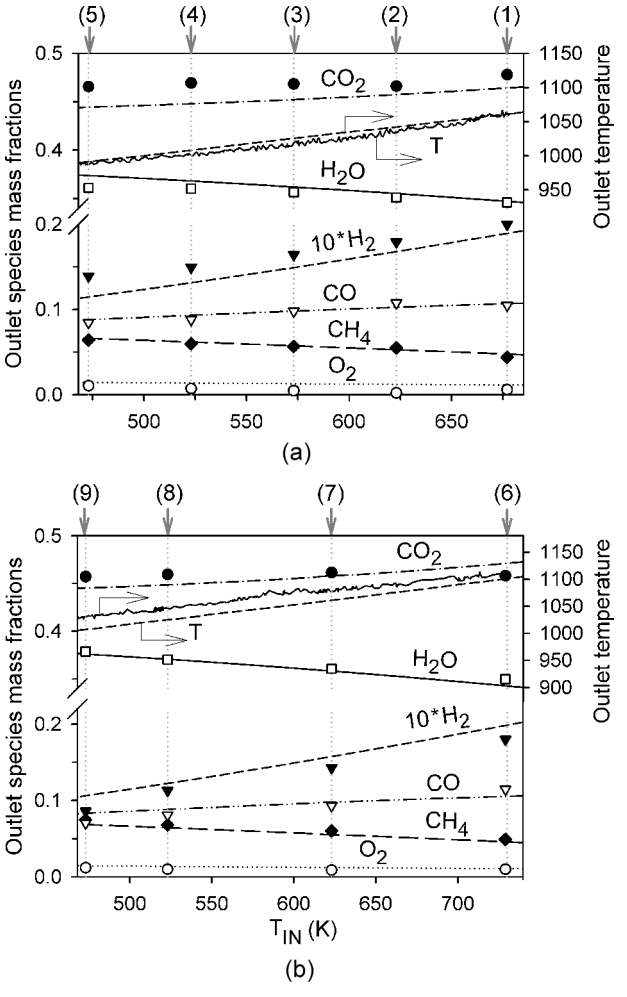

Figure 15 Predicted (lines) and measured (symbols) outlet species mass fractions for: (a) Cases 1 to 5 and (b) Cases 6 to 9. The symbol and line notation is the same as in Figure 6. The measured outlet temperature (solid line) at position E and the predicted outlet mean gas temperature (dashed line) are also shown.

Catalytic Extinction

Following catalytic ignition, vigorous burning states were established in Cases 1 and 6. Subsequently, the inlet temperature was ramped down so as to establish new steady states; at those steady states (typically every $\Delta T_{IN} = 50\,K$) detailed exhaust gas analysis was performed. Comparisons between predicted and measured exhaust gas compositions and temperatures for Cases 1 to 5 and Cases 6 to 9 are illustrated in Figure 15a and Figure 15b, respectively. Predictions were carried out with a steady-state version of the numerical code (Dogwiler et al., 1999; Schneider et al., 2006), whereby the steady solutions at higher inlet temperatures were used as an initial guess to obtain converged solutions at lower inlet temperatures (the lines in Figure 15 were constructed by successive steady computations at steps

$\Delta T_{IN} = 10\,K$). The complete transient process between measured steady states at different inlet temperatures was of no interest in the present investigation; moreover, it was computationally prohibitive to carry out transient simulations as the time span between the successive experimental steady states of Figure 15 exceeded 5 min. The temperature measurements in Figure 15 referred to thermocouple E and were continuous, whereas the corresponding predictions referred to the outlet ($x = 65\,mm$) mean gas temperature. The accuracy in the measurements of Figure 15 was particularly good: the C/H/O balances were better than 1% and the differences between inlet and outlet total enthalpies corresponded to an equivalent temperature differential of less than 15 K for all examined cases.

The lowest inlet temperature in the experiments was $T_{IN} = 473\,K$, for both the 1% Rh (Figure 15a) and the 0.5% Rh loading (Figure 15b). At $T_{IN} = 450\,K$ steady vigorous combustion was also attained, however, water condensation at the colder solid walls of the mixing section prohibited any further reduction of the inlet temperature. For a steam partial pressure of 2.3 bar (Cases 1 through 9), thermodynamics indicated that water should start condensing at about 400 K. Therefore, inlet temperatures below ca. 470 K were of no interest in practical CPO systems (e.g., gas turbines) with large EGR. Nonetheless, sustaining stable combustion at inlet temperatures as low as 470 K was of particular importance for part-load and idle turbine operation.

The resilience of CPO against extinction is explained next. When the inlet temperature decreased, there was a shift from partial to total oxidation regarding the H_2/H_2O species; this was manifested by the drop (rise) of the H_2 (H_2O) mass fraction in both experiments and predictions (Figure 15). The predicted H_2 selectivity (Eq. (16)) decreased substantially from 0.91 at $T_{IN} = 680\,K$ to 0.70 at $T_{IN} = 473\,K$. The CO and CO_2 mass fractions both decreased with decreasing inlet temperature, with the CO selectivity increasing modestly from 0.74 at $T_{IN} = 680\,K$ to 0.77 at $T_{IN} = 473\,K$. Overall, the presence of total oxidation products was more pronounced at lower temperatures (the reason being that reforming reactions were thermodynamically favored at higher temperatures). The increased importance of the total oxidation pathway with decreasing T_{IN} led, in turn, to higher reactor exothermicity that compensated–to a great extent–for the drop in inlet temperature. For example, the difference in exhaust gas temperatures at $T_{IN} = 473$ and 680 K (Cases 1 and 5 in Figure 15a) was only 70 K. Alternately, the computed heat release in Case 1 amounted to 45% of the heat release calculated when considering complete oxidation of methane; the corresponding number for Case 5 was 57%. It is finally noted that the agreement between measurements and predictions in Figure 15 was quite good: the predicted and measured species mass fractions were within 8% (the scarce O_2 was an exception) at $T_{IN} \geq 573$ and within 15% at $T_{IN} \leq 523$. The predicted outlet temperatures were within 12 K (Figure 15a) and 25 K (Figure 15b) of the measurements. At lower inlet temperatures, the model appeared to slightly overpredict (underpredict) the route to CO (CO_2).

Since water condensation prohibited the investigation of potential extinction at inlet temperatures below 473 K, additional experiments were carried out with $CH_4/O_2/N_2$ compositions without EGR (Cases 11 to 14); the O_2/N_2 molar ratio in those experiments was 0.24, close to that of air. The results of Figure 16 indicated that stable and vigorous combustion could be sustained even at room temperature ($T_{IN} = 298\,K$). The reason for the resilience against extinction was the same as in

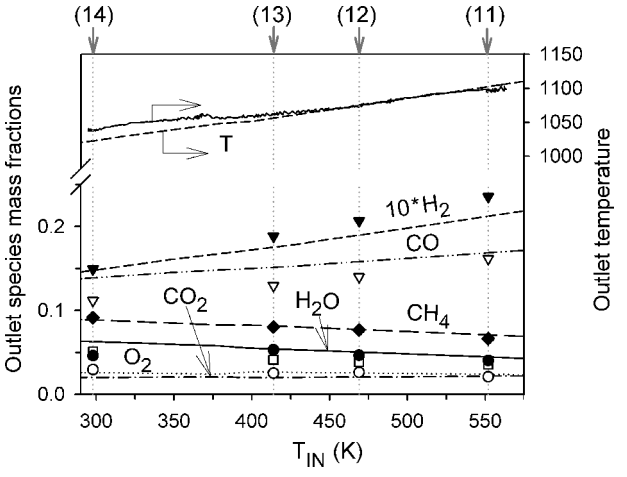

Figure 16 Predicted (lines) and measured (symbols) outlet species mass fractions for Cases 11 to 14 of Table 1. The symbol and line notation is the same as in Figure 6. The measured outlet temperature (solid line) at position E and the predicted outlet mean gas temperature (dashed line) are also shown.

the previous EGR-diluted cases: lower inlet temperatures favored the total over the partial oxidation route. It is worth pointing that recent experiments in a subscale gas-turbine CPO reactor (using various fuels with air) have also attested stable operation at room inlet temperature (Smith et al., 2005).

Ignition-Extinction Characteristics and Chemistry of Catalytic Extinction

Having established the applicability of the employed heterogeneous reaction mechanism, a rigorous numerical analysis of catalytic ignition-extinction has been carried out using the SPSR model of Eqs. (14) and (15). This analysis allowed for the investigation of residence times shorter than the $\sim$ 8–10 ms of the present experiments. The plots of Figure 17, obtained by continuation analysis, provided the ignition and extinction characteristics in terms of the weakly reacting and vigorous burning stable branches. The SPSR surface-to-volume ratio was 33.3 $cm^{-1}$and the residence times ranged from 1 to 8 ms; both CPO with EGR (Figure 17a) and CPO without EGR (Figure 17b) were investigated. In CPO with EGR (Figure 17a), a reduction in residence time led to higher inlet temperature requirements for the attainment of light-off. However, upon ignition, the established vigorous burning states had higher temperatures at shorter residence times. The reason was that shorter residence times favored the exothermic oxidation reactions of methane against the slower endothermic reforming reactions. By reducing the inlet temperature, extinction was obtained only for the $\tau = 1$ and 2 ms cases. For residence times $\tau \geq 4$ ms, vigorous combustion could be sustained down to $T_{IN} = 273$ K (water condensation was not considered herein). Therefore, extinction in CPO with EGR could only be an issue at very short reactor residence times that are not relevant to power generation cycles. For CPO without EGR, combustion could not be extinguished down to $T_{IN} = 273$ K, even at residence times as short as 1 ms (Figure 17b).

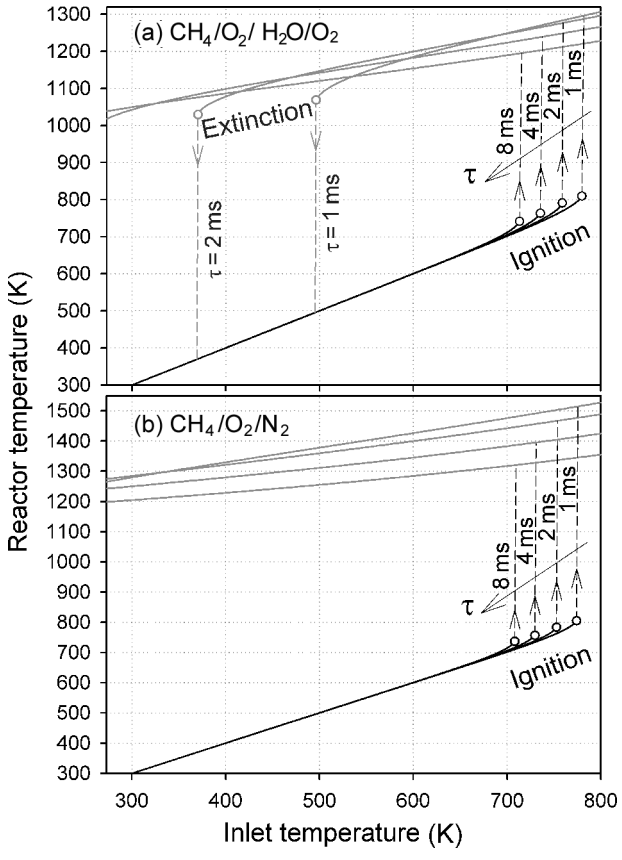

Figure 17 Ignition and extinction in an SPSR with a surface to volume ratio of 33.3 cm^{-1}, p = 5 bar and various residence times: (a) CH_4/O_2 mixtures with EGR, having inlet composition as Cases 1 to 9 of Table 1, and (b) $CH_4/O_2/N_2$ mixtures without EGR, having inlet composition as Cases 11 to 14 of Table 1. The black solid lines indicate the weakly reacting branch and the gray solid lines the vigorous burning branch.

The reactor temperatures were higher than those of CPO with EGR dilution, thus allowing for higher resilience against extinction.

The controlling surface chemistry during extinction in CPO with EGR was finally investigated. The normalized sensitivity coefficients of the most important reactions affecting the SPSR temperature, the methane mass fraction, and the Rh(s) coverage are provided in Figure 18. The sensitivity analysis of Figure 18 (carried out on the fly during the construction of the continuation plots) pertained to the $\tau = 2$ ms case of Figure 17a, with expanded details around the extinction temperature $T_e = 370.3$ K. The key parameter controlling extinction was the CO(s) coverage. The main coverage at high temperatures was Rh(s) and CO(s) (see also Figure 7). By decreasing the reactor temperature, CO(s) increased leading to a catalyst poisoning due to the corresponding reduction of available free sites. All reactions shown in Figure 18 had a direct impact on the CO(s) coverage. Reactions S6 and S36 were the adsorption and desorption of CO; an increase (decrease) of S6 (S36) led to a drop

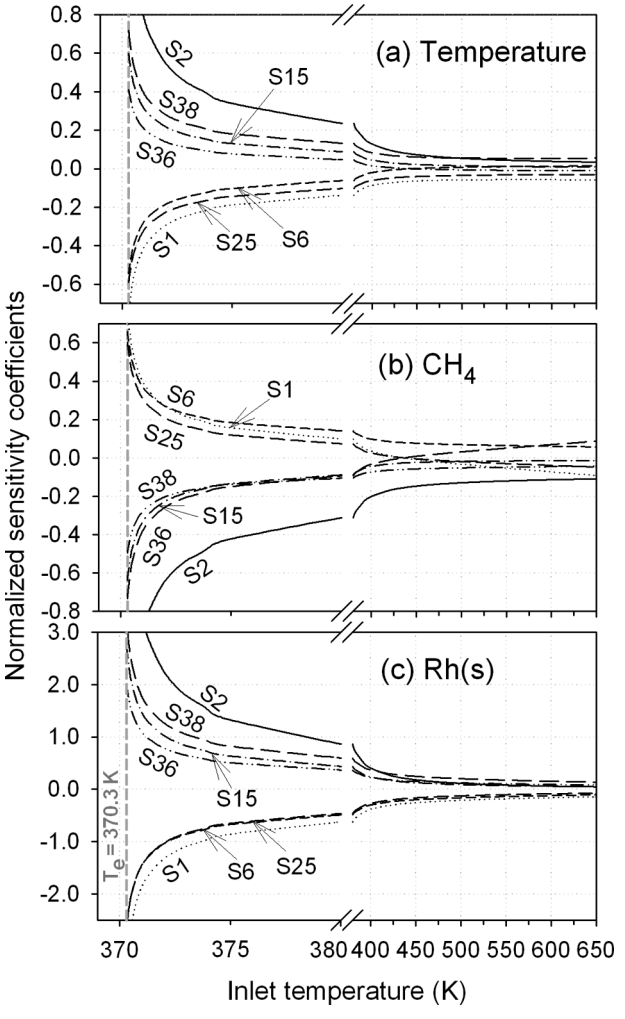

Figure 18 Normalized sensitivity coefficients of the most sensitive reactions on (a) reactor temperature, (b) CH_4 concentration, and (c) Rh(s) surface coverage, versus SPSR inlet temperature. SPSR surface-to-volume ratio $S/V = 33.3\,cm^{-1}$, $p = 5$ bar, and $\tau = 2$ ms. The inlet composition is the same as in Cases 1 to 9 of Table 1. Details are shown around the extinction point of Figure 17(a) with inlet temperature 370.3 K and residence time 2 ms. The reaction numbering follows Table 3.

in reactor temperature and Rh(s) coverage (Figures 18a, 18c), and to a rise in methane levels (Figure 18b), thus promoting extinction.

Reaction S15 depleted CO(s) by surface oxidation to CO_2(s); hence an increase in the rate of S15 stabilized combustion. The adsorption/desorption of CH_4 (S1/S38) and the surface oxidation of CH_4(s) (S25) played also key roles since they provided the surface carbon needed to build CO(s). A reduction (increase) of the methane adsorption (desorption) extended the extinction limits; for example, a two-fold decrease in the sticking coefficient of methane yielded a twofold decrease in

CO(s) coverage that in turn provided stable vigorous combustion at inlet temperatures as low as 308 K. Finally, an increase in O_2 adsorption (S2) near extinction extended the combustion stability limits since it enhanced the free site coverage Rh(s) at the expense of CO(s) by promoting the surface oxidation reaction S15. It is worth pointing that the CO chemistry, which was found important for catalytic extinction, also controlled catalytic ignition (see Figure 9 and related discussion).

CONCLUSIONS

The ignition and extinction in catalytic partial oxidation (CPO) of CH_4/O_2 mixtures with large EGR (exhaust gas recycle, comprising 46.3% H_2O and 23.1% CO_2 vol.) has been investigated experimentally and numerically at 5 bar. In addition, the extinction in CPO of $CH_4/O_2/N_2$ mixtures was studied at 3 bar. Experiments have been carried out in a Rh-coated short contact time honeycomb catalytic reactor and included thermocouple measurements of the reactor temperature and exhaust gas analysis. Numerical predictions were performed with a 2-D transient elliptic code. The following are the key conclusions of this study.

1. The employed heterogeneous reaction scheme reproduced the measured minimum inlet temperatures required for light-off, the elapsed times for the propagation of the reaction front, and the steady-state exhaust gas compositions in CPO with EGR at a fuel-to-oxygen equivalence ratio $\varphi = 4.0$. At $\varphi = 2.5$, however, only qualitative agreement was obtained and the numerical model overpredicted the synthesis gas yields.
2. The chemical impact of the added H_2O in the feed was already evident at the early stages of the transient catalytic ignition event and its importance further increased as steady state was approached. At steady state, the large H_2O dilution resulted in increased hydrogen selectivity, decreased CO selectivity and slightly increased methane conversion. The chemical impact of CO_2 dilution was minimal on both the transient event and the subsequent steady combustion.
3. Despite the significant chemical impact of H_2O dilution during the light-off process, the ignition delay times themselves were practically unaffected by its presence. The reason was that light-off times were dominated by total oxidation reactions and not by partial oxidation or reforming reactions leading to synthesis gas products. The key reaction affecting catalytic ignition was the surface oxidation of CO to CO_2, which was the main exothermic heat release step in the induction zone. The surface oxidation of H_2 to H_2O, on the other hand, was less significant due to the low amounts of H_2 formed in the induction zone.
4. Measurements and predictions indicated that vigorous combustion could be sustained at inlet temperatures as low as 473 K in CPO with EGR. In CPO without EGR, vigorous combustion was still possible with inlet temperatures as low as 298 K. The reason for the extended stability limits of CPO combustion was the shift from partial to total oxidation products–and hence to higher exothermicity-with decreasing inlet temperature.
5. Computed extinction characteristics obtained at various reactor residence times indicated that extinction in CPO with EGR was possible only at very short times (<4 ms), which were not relevant to new power generation cycles. On the other

hand, in CPO without EGR stable combustion was attained at residence times as short as 1 ms. The key parameter controlling catalytic extinction in CPO was the CO(s) coverage. Near extinction CO(s) increased, reducing the free sites and thus leading to catalyst poisoning.

6. The advantage of reactor materials with high thermal conductivity has been demonstrated for practical CPO systems. Moreover, operation at non-optimal stoichiometries ($\varphi = 2.5$) was shown to be beneficial in CPO with large EGR, due to the moderating effects of dilution on the maximum reactor temperature.

NOMENCLATURE

Notation

B	ratio of active to geometrical surface area
c_p, c	specific heat of gas at constant pressure, specific heat of solid
D_{km}	mixture-average diffusion coefficient of k-th species
D_k^T	thermal diffusion coefficient of k-th species
h	total enthalpy of gaseous mixture
h_k, h_k°	total and chemical enthalpy of k-th species
K_g	total number of gas-phase species
L, L_c, L_u	total reactor length, coated length, uncoated length
M_s	total number of surface species
p	pressure
$\dot{q}_{\mathrm{acc}}$, $\dot{q}_{\mathrm{gen}}$	heat accumulation and heat generation
$\dot{q}_{\mathrm{rad}}$, $\dot{q}_{\mathrm{cond}}$, $\dot{q}_{\mathrm{conv}}$	radiative, conductive and convective heat transfer
R	universal gas constant
Re	Reynolds number
r_h	channel hydraulic radius
$\dot{s}_k$	heterogeneous molar production rate of k-th species
S_k	selectivity of k-th species
S/V	surface-to-volume ratio
t	time
T	temperature
T_{o}, T_{eq}	reference temperature, adiabatic equilibrium temperature
u, U_{IN}	axial velocity component, inlet axial velocity
v	radial velocity component
$\vec{V}_k$	diffusion velocity vector of k-th gaseous species
W_k, $\overline{W}$	species molecular weight, average molecular weight
X_k, Y_k	gas-phase species mole and mass fraction
x, r	streamwise and radial coordinates

Greek Symbols

α	thermal diffusivity ($\lambda/\rho\ c$)
Γ	surface site density
δ, δ_{c}	channel wall thickness, catalyst layer thickness
ε	surface emissivity
θ_{m}	surface species coverage
λ	thermal conductivity
μ	viscosity
ρ	density
σ_{m}	surface species site occupancy
τ	reactor residence time
φ	fuel-to-air equivalence ratio
$\dot{\omega}_k$	gas-phase molar production rate of k-th species

Subscripts

IN, OUT	inlet, outlet
g	gas
FeCr, ZrO_2	solid materials
k, *m*	indices for gas-phase and surface species
W	wall
x, *r*	streamwise and radial components

Abbreviations

CPO	catalytic partial oxidation
EGR	exhaust gas recycle
GHSV	gas hourly space velocity
SPSR	surface perfectly stirred reactor

REFERENCES

Aghalayam, P., Park, Y.K., Fernandes, N., Papavassiliou, V., Mhadeshwar, A.B., and Vlachos, D.G. (2003) A C1 mechanism for methane oxidation on platinum. *J. Catal.*, **213**, 23–38.

Appel, C., Mantzaras, J., Schaeren, R., Bombach, R., Inauen, A., Kaeppeli, B., Hemmerling, B., and Stampanoni, A. (2002) An experimental and numerical investigation of homogeneous ignition in catalytically stabilized combustion of hydrogen/air mixtures over platinum. *Combust. Flame*, **128**, 340–368.

Appel, C., Mantzaras, J., Schaeren, R., Bombach, R., Inauen, A., Tylli, N., Wolf, M., Griffin, T., Winkler, D., and Carroni, R. (2005) Partial catalytic oxidation of methane to synthesis gas over rhodium: In situ raman experiments and detailed simulations. *Proc. Combust. Instit.*, **30**, 2509–2517.

Bodke, A.S., Bharadwaj, S.S., and Schmidt, L.D. (1998) The effect of ceramic supports on partial oxidation of hydrocarbons over noble metal coated monoliths. *J. Catal.*, **179**, 138–149.

Carroni, R., Schmidt, V., and Griffin, T. (2002) Catalytic combustion for power generation. *Catal. Today*, **75**, 287–295.

Carroni, R., Griffin, T., Mantzaras, J., and Reinke, M. (2003) High-pressure experiments and modeling of methane/air catalytic combustion for power generation applications. *Catal. Today*, **83**, 157–170.

Coltrin, M.E., Kee, R.J., and Rupley, F.M. (1996) Surface Chemkin: A Fortran package for analyzing heterogeneous chemical kinetics at the solid surface-gas phase interface, Sandia National Laboratories, Report No. SAND90–8003C.

Deutschmann, O., Schmidt, R., Behrendt, F., and Warnatz, J. (1996) Numerical Modeling of Catalytic Ignition. *Proc. Combust. Instit.*, **26**, 1747–1754.

Deutschmann, O. and Schmidt, L.D. (1998) Modeling the partial oxidation of methane in a short-contact-time reactor. *AIChE J.*, **44**, 2465–2477.

Dogwiler, U., Benz, P., and Mantzaras, J. (1999) Two-dimensional modelling for catalytically stabilized combustion of a lean methane-air mixture with elementary homogeneous and heterogeneous chemical reactions. *Combust. Flame*, **116**, 243–258.

Eriksson, S., Wolf, M., Schneider, A., Mantzaras, J., Raimondi, F., Boutonnet, M., and Järas, S. (2006) Fuel rich catalytic combustion of methane in zero emissions power generation processes. *Catal. Today*, **117**, 447–453.

Ferziger, J.H. and Petric, M. (1999) Computational Methods for Fluid Dynamics, Springer Verlag, New York, p. 142.

Griffin, T., Winkler, D., Wolf, M., Appel, C., and Mantzaras, J. (2004) Staged catalytic combustion method for the advanced zero emissions gas turbine power plant. ASME Gas Turbine Expo, paper GT2004–54101.

Griffin, T., Sundkvist, S.G., Asen, K.I., and Bruun, T. (2005) Advanced zero emission gas turbine power plant. *J. Eng. Gas Turbines Power*, **127**, 81–85.

Hickman, D.A. and Schmidt, L.D. (1993) Steps in CH_4 oxidation on Pt and Rh surfaces: high-temperature reactor simulations. *AIChE J*, **39**, 1164–1177.

Imbihl, R. and Ertl, G. (1995) Oscillatory kinetics in heterogeneous catalysis. *Chem. Rev.*, **95**, 697–733.

Karagiannidis, S., Mantzaras, J., Jackson, G., and Boulouchos, K. (2007) Hetero-/homogeneous combustion and stability maps of methane-fueled catalytic microreactors. *Proc. Combust. Instit.*, **31**, 3309–3317.

Karim, H., Lyle, K., Etemad, S., Smith, L., Pfefferle, W.C., Dutta, P., and Smith, K. (2002) Advanced catalytic pilot for low NOx industrial gas turbines. ASME Gas Turbine Expo, paper GT2002-30083.

Kee, R.J., Dixon-Lewis, G., Warnatz, J., Coltrin, M.E., and Miller, J.A. (1996a) A Fortran computer code package for the evaluation of gas-phase multicomponent transport properties, Sandia National Laboratories, Report No. SAND86-8246.

Kee, R.J., Rupley, F.M., and Miller, J.A. (1996b) Chemkin II: A Fortran chemical kinetics package for the analysis of gas-phase chemical kinetics, Sandia National Laboratories, Report No. SAND89-8009B.

Kramer, J.F., Reihani, S.A.S., and Jackson, G.S. (2002) Low temperature combustion of hydrogen on supported pd catalysts. *Proc. Combust. Instit.*, **29**, 989–996.

Lutz, A.E., Kee, R.J., and Miller, J.A. (1996) SENKIN: A Fortran program for predicting homogeneous gas phase chemical kinetics with sensitivity analysis, Sandia National Laboratories, Report No. SAND87-8248.

Mantzaras, J., Appel, C., Benz, P., and Dogwiler, U. (2000) Numerical modelling of turbulent catalytically stabilized channel flow combustion. *Catal. Today*, **53**, 3–17.

Mantzaras, J. (2006) Understanding and modeling of thermofluidic processes in catalytic combustion. *Catal. Today*, **117**, 394–406.

Mark, M.F. and Maier, W.F. (1996) CO_2-reforming of methane on supported Rh and Ir catalysts. *J. Catal.*, **164**, 122–130.

Moffat, H.K., Kee, R.J., Grcar, J.F., and Miller, J.A. (1993) Surface PSR: A Fortran program for modeling well-stirred reactors with gas and surface reactions, Sandia National Laboratories, Report No. SAND91–8001.

Patankar, S.V. (1980) Numerical Heat Transfer and Fluid Flow. Hemisphere Publ. Corp., New York.

Reinke, M., Mantzaras, J., Schaeren, R., Bombach, R., Inauen, A., and Schenker, S. (2004) High-pressure catalytic combustion of methane over platinum: In situ experiments and detailed numerical predictions. *Combust. Flame*, **136**, 217–240.

Reinke, M., Mantzaras, J., Bombach, R., Schenker, S., and Inauen, A. (2005) Gas phase chemistry in catalytic combustion of methane/air mixtures over platinum at pressures of 1 bar to 16 bar. *Combust. Flame*, **141**, 448–468.

Schneider, A., Mantzaras, J., and Jansohn, P. (2006) Experimental and numerical investigation of the catalytic partial oxidation of CH_4/O_2 mixtures diluted with H_2O and CO_2 in a short contact time reactor. *Chem. Eng. Sci.*, **61**, 4634–4646.

Schneider, A., Mantzaras, J., Bombach, R., Schenker, S., Tylli, N., and Jansohn, P. (2007) Laser induced fluorescence of formaldehyde and raman measurements of major species during partial catalytic oxidation of methane with large H_2O and CO_2 dilution at pressures up to 10 bar. *Proc. Combust. Instit.*, **31**, 1973–1981.

Schwiedernoch, R., Tischer, S., Correa, C., Deutschmann, O., and Warnatz, J. (2002) Experimental and numerical investigation of the ignition of methane combustion in a platinum-coated honeycomb monolith. *Proc. Combust. Instit.*, **29**, 1005–10011.

Schwiedernoch, R., Tischer, S., Correa, C., and Deutschmann, O. (2003) Experimental and numerical study on the transient behavior of partial oxidation of methane in a catalytic monolith. *Chem. Eng. Sci.*, **58**, 633–642.

Siegel, R. and Howell, J.R. (1981) Thermal Radiation Heat Transfer, Hemisphere, New York, p. 271.

Sinha, N., Bruno, C., and Bracco, F.V. (1985) Two-dimensional, transient catalytic combustion of CO-Air on platinum. *Physicochem. Hydrodyn.*, **6**, 373–391.

Smith, L.L., Karim, H., Castaldi, M.J., Etemad, S., and Pfefferle, W.C. (2006) Rich-catalytic lean-burn combustion for fuel-flexible operation with ultra-low emissions. *Catal. Today*, **117**, 438–446.

Smith, L.L., Karim, H., Castaldi, M.J., Etemad, S., and Pfefferle, W.C. (2005) Fuel-flexible fuel-rich catalytic combustion with ultra-low emissions. Paper presented at the Sixth International Workshop on Catalytic Combustion (IWCC6), Ischia, Italy, September 11–14.

Touloukian, Y.S., Powell, R.W., Ho, C.Y., and Klemens, P.G. (1970) Thermal conductivity: metallic elements and alloys. Touloukian Y.S. and Ho, C.Y. (Eds.) *Thermophysical Properties of Matter*, TPRC Data Series, Plenum, New York.

Veser, G., Ziauddin, M., and Schmidt, L.D. (1999) Ignition in alkane oxidation on noble-metal catalysts. *Catal. Today*, **47**, 219–228.

Veser, G. and Frauhammer, J. (2000) Modelling steady state and ignition during catalytic methane oxidation in a monolith reactor. *Chem. Eng. Sci.*, **55**, 2271–2286.

Warnatz, J., Dibble, R.W., and Maas, U. (1996) Combustion, Physical and Chemical Fundamentals, Modeling and Simulation, Springer-Verlag, New York.

Zygourakis, K. (1989) Transient operation of monolith catalytic converters: A two-dimensional reactor model and the effects of radially nonuniform flow distributions. *Chem. Eng. Sci.*, **44**, 2075–2086.